Copyright © 2013 Tech Science Press CMES, vol.96, no.1, pp.49-90, 2013

A Direct Forcing Immersed Boundary Method Employed With Compact Integrated RBF Approximations For Heat Transfer and Fluid Flow Problems

N. Thai-Quang[1], N. Mai-Duy[1], C.-D. Tran[1] and T. Tran-Cong[1,2]

Abstract: In this paper, we present a numerical scheme, based on the direct forcing immersed boundary (DFIB) approach and compact integrated radial basis function (CIRBF) approximations, for solving the Navier-Stokes equations in two dimensions. The problem domain of complicated shape is embedded in a Cartesian grid containing Eulerian nodes. Non-slip conditions on the inner boundaries, represented by Lagrangian nodes, are imposed by means of the DFIB method, in which a smoothed version of the discrete delta functions is utilised to transfer the physical quantities between two types of nodes. The velocities and pressure variables are approximated locally on Eulerian nodes using 3-node CIRBF stencils, where first- and second-order derivative values of the field variables are also included in the RBF approximations. The present DFIB-CIRBF scheme is verified through the solution of several test problems including Taylor-Green vortices, rotational flow, lid-driven cavity flow with multiple solid bodies, flow between rotating circular and fixed square cylinders, and natural convection in an eccentric annulus between two circular cylinders. Numerical results obtained using relatively coarse grids are in good agreement with available data in the literature.

Keywords: compact integrated RBF, immersed boundary, direct forcing, viscous flow, heat transfer.

1 Introduction

Flows past solid bodies of arbitrary shapes are widely encountered in engineering applications. Body-fitted grid methods, where the governing equations are discretised on a curvilinear grid conforming to the boundary, have been applied to solve

---

[1] Computational Engineering and Science Research Centre, Faculty of Health, Engineering and Sciences, The University of Southern Queensland, Toowoomba, Queensland 4350, Australia.

[2] Corresponding author. Email: thanh.tran-cong@usq.edu.au. Tel: +61 7 4631 1332. Fax: +61 7 4631 2110.

such problems. Their main advantage is that the boundary conditions can be imposed in a simple and accurate way. However, generating a high quality mesh/grid is difficult and time-consuming. As a result, a lot of research effort has been spent on the development of non-body-conforming methods. Among them, the immersed boundary methods (IBMs) have received much attention in recent years. In IBMs, one joins the fluid and solid regions together to make a single domain that is discretised using a Cartesian grid. This approach greatly simplifies the process of mesh generation and also retains the relative simplicity of the governing equations. The basis of IBMs lies in the way to introduce forces into the governing equations to impose prescribed values on the immersed boundary.

The IBM was originally introduced by Peskin (1977) to investigate the fluid dynamics of blood flow in human heart. The flow field is defined on the Eulerian coordinates, while the boundaries are represented on the Lagrangian coordinates. The singular forces on the boundaries are known, and their effects on the flow field are taken into account via regularised Dirac delta functions. Since then, many variants of the Peskin's method have been proposed. Goldstein, Handler, and Sirovich (1993) developed a feedback forcing approach to iteratively determine the magnitude of the force required to obtain a desired velocity on the immersed boundary. Saiki and Biringen (1996) implemented this approach with the virtual boundary method (VBM) to compute the flow past a stationary, rotating and oscillating circular cylinder. However, the feedback forcing approach induces some oscillations and places some restriction on the computational time step. To overcome these drawbacks, Fadlun, Verzicco, Orlandi, and Mohd-Yusof (2000) proposed an approach, namely the direct forcing (DF) technique, to evaluate the interactive forces between the immersed boundary (IB) and the fluid, which is equivalent to applying a forcing term to the Navier-Stokes equations. In comparison with the feedback forcing approach, the DF approach can work with larger computational time steps. Kim, Kim, and Choi (2001) proposed a combined IB finite-volume method, where a mass source/sink and a momentum forcing are introduced, for simulating flows over complex geometries. To transfer the physical quantities smoothly between Eulerian and Lagrangian nodes and avoid strong restrictions on the time step, Uhlmann (2005) presented a method to incorporate the regularised delta functions into a direct formulation of the fluid-solid interactive force. Wang, Fan, and Luo (2008) developed an explicit multi-direct forcing approach and obtained a better satisfaction of the non-slip boundary condition than the original DF approach. Recently, Ji, Munjiza, and Williams (2012) proposed an iterative IBM in which the body force updating is incorporated into the pressure iterations for the two- (2D) and three-dimensional (3D) numerical simulations of laminar and turbulent flows. The reader is referred to, e.g., Mittal and Iaccarino (2005) for a comprehensive review of IBMs.

High-order approximation schemes for the Navier-Stokes equations have the ability to provide efficient solutions to steady/unsteady fluid flow problems. A high level of accuracy can be achieved using a relatively coarse discretisation. Many types of high-order schemes for the Navier-Stokes equations have been reported in the literature. Botella and Peyret (1998) developed a Chebyshev collocation method and provided the benchmark results for the lid-driven cavity flow problem. Ding, Shu, Yeo, and Xu (2006) presented a local multiquadric differential quadrature method for the solution of 3D incompressible flow problems in the velocity-pressure formulation, while Mai-Duy and Tran-Cong (2001b), Mai-Duy, Le-Cao, and Tran-Cong (2008), Mai-Duy and Tran-Cong (2008), Le-Cao, Mai-Duy, and Tran-Cong (2009) proposed an integrated-RBF (IRBF) method to solve heat transfer and fluid flow problems in the stream function-vorticity formulation. Recently, Tian, Liang, and Yu (2011) proposed a fourth-order compact difference scheme constructed on 2D nine-point stencils, and Fadel and Agouzoul (2011) used the standard Padé scheme to construct high-order approximations for the velocity-pressure-pressure gradient formulation. It is noted that the velocity ($\mathbf{u}$) and pressure (p) formulation has several advantages over the stream function-vorticity formulation and the stream function formulation. The $\mathbf{u}$-p formulation can provide the velocity and pressure fields directly from solving the discretised equations and also work for 2D and 3D problems in a similar manner.

RBF networks (RBFNs) have emerged as a powerful approximation tool. The application of RBFNs for the solution of ordinary (ODEs) and partial (PDEs) differential equations was first presented by Kansa (1990). Mai-Duy and Tran-Cong (2001a) proposed the use of integration, instead of the usual differentiation, to construct the RBFN expressions (IRBFNs) in order to avoid the reduction of convergence rate. IRBFNs were developed into global one-dimensional forms (1D-IRBF) for second- and fourth-order PDEs [Mai-Duy and Tanner (2007)] and compact local forms for second-order elliptic problems [Mai-Duy and Tran-Cong (2011); Mai-Duy and Tran-Cong (2013)]. For the latter, the information about the governing equation or derivatives of the field variable is also included in local approximations to enhance the solution accuracy.

In this paper, we present a numerical scheme, namely DFIB-CIRBF, for solving unsteady/steady fluid flow problems in 2D. The present scheme combines the direct forcing immersed boundary (DFIB) method and the high-order compact integrated radial basis function (CIRBF) approximations for the spatial discretisation and utilises the second-order Adams-Bashforth/Crank-Nicolson algorithms for the temporal discretisation. An interactive force, representing the effect of the solid bodies on the fluid region, is added directly to the governing equations (i.e. direct forcing) on the fluid-solid regions to satisfy their boundary conditions. This interactive force is evaluated explicitly from the pressure gradient, the convection and diffusion terms in the previous time level. Because the Eulerian grid nodes do not generally coincide with the nodes on the interfaces represented by Lagrangian nodes, a smoothed version of the discrete delta functions is employed to transfer the quantities between two types of nodes. The CIRBF approximations are constructed over 3-point stencils, where nodal first- and second-order derivative values of the field variables are included in the RBF approximations [Thai-Quang, Mai-Duy, Tran, and Tran-Cong (2012)]. A series of test problems, including Taylor-Green vortices, rotational flow, flow between rotating circular and fixed square cylinders, and natural convection in an eccentric annulus between two circular cylinders, is considered to verify the present scheme. The remainder of the paper is organised as follows. Section 2 outlines the equations which govern the fluid flow phenomena. The numerical formulation including the derivation of interactive forces, and the temporal and spatial discretisations is described in detail in Section 3. In Section 4, in order to evaluate the efficiency of the present method, several numerical results are presented and compared with the analytic solutions and some approximate results available in the literature, where appropriate. Section 5 concludes the paper.

2 Governing equations

The IB approach takes the Navier-Stokes equation for thermal flows in the dimensionless form as follows

$$\nabla.\mathbf{u} = 0 \quad \text{in} \quad \Omega, \tag{1}$$

$$\frac{\partial \mathbf{u}}{\partial t} + (\mathbf{u}.\nabla)\mathbf{u} = -\nabla p + \sqrt{\frac{Pr}{Ra}}\nabla^2\mathbf{u} + \mathbf{f}_b + \mathbf{f}_I \quad \text{in} \quad \Omega, \tag{2}$$

$$\frac{\partial T}{\partial t} + (\mathbf{u}.\nabla)T = \frac{1}{\sqrt{PrRa}}\nabla^2 T + f_{I,T} \quad \text{in} \quad \Omega, \tag{3}$$

subject to the initial and boundary conditions:

$$\mathbf{u}(x,y,0) = \mathbf{u}_0(x,y) \quad \text{in} \quad \Omega, \tag{4}$$

$$T(x,y,0) = T_0(x,y) \quad \text{in} \quad \Omega, \tag{5}$$

$$\mathbf{u}(x,y,t) = \mathbf{u}_\Gamma(x,y,t) \quad \text{on} \quad \Gamma, \tag{6}$$

$$T(x,y,t) = T_\Gamma(x,y,t) \quad \text{on} \quad \Gamma, \tag{7}$$

where Ω is the entire domain of analysis that is of simpler shape than the fluid domain; $\mathbf{u} = (u,v)^T$, p and T the velocity vector, the static pressure and the temperature, respectively; $\mathbf{f}_b = \left(f_{b,x}, f_{b,y}\right)^T$, $\mathbf{f}_I = (f_{I,x}, f_{I,y})^T$ and $f_{I,T}$ the body-force vector, the momentum interactive force vector and the thermal interactive force, respectively; $\mathbf{u}_0$, $\mathbf{u}_\Gamma$, T_0 and T_Γ prescribed functions; Pr and Ra the Prandtl and Rayleigh numbers defined as $Pr = \nu/\alpha$ and $Ra = \beta g \Delta T L^3/\alpha\nu$, respectively, in which ν is the kinematic viscosity, α is thermal diffusivity, β the thermal expansion coefficient, g the gravity and L and ΔT the characteristic length and temperature difference, respectively. In the dimensionless form, the characteristic velocity is taken as $U_0 = \sqrt{gL\beta\Delta T}$ for the purpose of balancing the buoyancy and inertial forces.

In (1), (2) and (3), the field variables are made dimensionless according to the following definitions

$$x = \frac{x'}{L},\ y = \frac{y'}{L},\ u = \frac{u'}{U_0},\ v = \frac{v'}{U_0},\ p = \frac{p'}{\rho U_0^2},\ T = \frac{T' - T_c}{T_h - T_c}, \tag{8}$$

where x', y', u', v', p', T' are the corresponding dimensional variables; and T_h and T_c the hot and cold temperatures, respectively.

The interactive forces $\mathbf{f}_I$ and $f_{I,T}$ represent the influence of the immersed solid bodies on the fluid by the viscous and thermal effects, while the body force $\mathbf{f}_b$ is a function of the temperature, for instance, $\mathbf{f}_b = (0,T)^T$ for the thermal problem considered in Section 4. For isothermal flows, the term $\mathbf{f}_b$ in (2) is set to null, equation (3) is deactivated and the term $\sqrt{\frac{Pr}{Ra}}$ in (2) is replaced by $\frac{1}{Re}$ where $Re = U_0 L/\nu$ is the Reynolds number.

3 Numerical formulation

Consider a domain Ω comprised of the fluid region Ω_f and solid region Ω_s. The latter is composed of N_{esb} embedded solid bodies S_k $\left(\Omega_s = \bigcup_{k=1}^{N_{esb}} S_k\right)$ as shown in Figure 1. Let Γ and ∂S_k be the boundaries of Ω and kth solid body S_k, respectively. While the entire domain Ω is discretised using a fixed uniform Cartesian grid g_h containing Eulerian grid nodes $\mathbf{x}_{i,j} = (x_{i,j}, y_{i,j})^T$ $(i \in \{1,2,\ldots,n_x\}$ and $j \in \{1,2,\ldots,n_y\})$, each ∂S_k is described by a set of N_L^k Lagrangian nodes

$$\mathbf{X}_l^k = \left(X_l^k, Y_l^k\right)^T \in \partial S_k \quad 1 \le l \le N_L^k,\ 1 \le k \le N_{esb}. \tag{9}$$

3.1 Direct forcing method

It can be seen that the Lagrangian nodes, representing the immersed boundaries, do not generally coincide with the fixed Eulerian nodes on the computational domain Ω. The direct forcing (DF) method, a variant of the IB approach, takes into account non-slip and thermal boundary conditions on the fluid-solid interfaces by

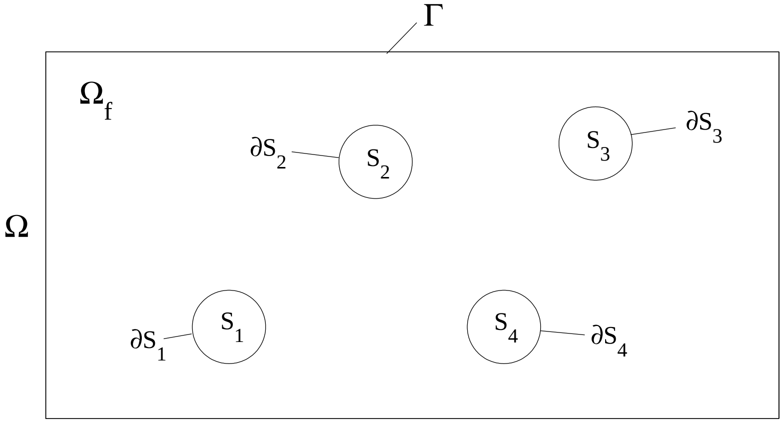

Figure 1: A schematic outline for the problem domain.

using the momentum interactive force $\mathbf{f}_I$ and the thermal interactive force $f_{I,T}$ to impose desired velocity and temperature values, respectively, at selected Eulerian nodes near the IB. An interpolation process is necessary to transfer data between the selected Eulerian nodes and the Lagrangian nodes on the IB. Below are the details for computing the momentum interactive force $\mathbf{f}_I$ in (2). One can calculate the thermal interactive force $f_{I,T}$ in (3) in a similar manner.

3.1.1 Derivation of the momentum interactive force

A temporal discretisation of the momentum equation (2) is given by Uhlmann (2005)

$$\frac{\mathbf{u}^n - \mathbf{u}^{n-1}}{\Delta t} = \mathbf{rhs}^{n-1/2} + \mathbf{f}_I^{n-1/2}, \tag{10}$$

where the superscript n denotes the current time level; the convection, pressure, diffusion and body-force terms at a time $t^{n-1/2}$ are lumped together in $\mathbf{rhs}^{n-1/2}$. The interactive force term yielding the desired velocity $\mathbf{u}^{(d)}$ can thus be defined as [Fadlun, Verzicco, Orlandi, and Mohd-Yusof (2000)]

$$\mathbf{f}_I^{n-1/2} = \frac{\mathbf{u}^{(d),n} - \mathbf{u}^{n-1}}{\Delta t} - \mathbf{rhs}^{n-1/2}, \tag{11}$$

at some selected nodes (and zero elsewhere). The corresponding interactive force at the Lagrangian nodes will be

$$\mathbf{F}_I^{n-1/2} = \frac{\mathbf{U}^{(d),n} - \mathbf{U}^{n-1}}{\Delta t} - \mathbf{RHS}^{n-1/2}. \tag{12}$$

Hereafter, we use upper-case letters for quantities evaluated at the Lagrangian nodes $\mathbf{X}_l^k$.

The desired velocity at a node on the fluid-solid interface in (12) is computed from the rigid-body motion of the solid body as follow

$$\mathbf{U}^{(d)}(\mathbf{X}_l^k) = \mathbf{U}_c^k + \boldsymbol{\omega}_c^k \times (\mathbf{X}_l^k - \mathbf{X}_c^k), \tag{13}$$

where $\mathbf{U}_c^k = \left(U_c^k, V_c^k\right)^T$, $\boldsymbol{\omega}_c^k$ and $\mathbf{X}_c^k$ are the translational velocity, rotational velocity and the position vectors of the mass centre of the *k*th solid body, respectively - all is defined in the Cartesian coordinate system.

When the interactive force is absent, equation (12) leads to

$$\widetilde{\mathbf{U}}^n = \mathbf{U}^{n-1} + \mathbf{RHS}^{n-1/2}\Delta t, \tag{14}$$

where $\widetilde{\mathbf{U}}^n$ is a preliminary velocity. Its Eulerian counterpart is

$$\widetilde{\mathbf{u}}^n = \mathbf{u}^{n-1} + \mathbf{rhs}^{n-1/2}\Delta t. \tag{15}$$

In the present work, we employ the Adams-Bashforth scheme for the temporal discretisation. The term $\mathbf{rhs}^{n-1/2}$ in (15) is computed explicitly as [Butcher (2003)]

$$\begin{aligned}\mathbf{rhs}^{n-1/2} = &- \left[\frac{3}{2}\nabla p^{n-1} - \frac{1}{2}\nabla p^{n-2}\right] - \left[\frac{3}{2}(\mathbf{u}^{n-1}.\nabla)\mathbf{u}^{n-1} - \frac{1}{2}(\mathbf{u}^{n-2}.\nabla)\mathbf{u}^{n-2}\right] \\ &+ \sqrt{\frac{Pr}{Ra}}\left[\frac{3}{2}\nabla^2\mathbf{u}^{n-1} - \frac{1}{2}\nabla^2\mathbf{u}^{n-2}\right] + \left[\frac{3}{2}\mathbf{f}_b^{n-1} - \frac{1}{2}\mathbf{f}_b^{n-2}\right].\end{aligned} \tag{16}$$

Then, the interactive force at the Lagrangian nodes is computed now as

$$\mathbf{F}_I^{n-1/2} = \frac{\mathbf{U}^{(d),n} - \widetilde{\mathbf{U}}^n}{\Delta t}. \tag{17}$$

In order to complete the evaluation of the interactive force term in (10), a mechanism for transferring the preliminary velocities ($\widetilde{\mathbf{u}}^n, \widetilde{\mathbf{U}}^n$) and the forces ($\mathbf{F}_I^{n-1/2}$, $\mathbf{f}_I^{n-1/2}$) between the two Eulerian and Lagrangian node systems is required.

3.1.2 Transfer of quantities between Eulerian and Lagrangian nodes

Peskin (2002) employed the class of regularised delta functions

$$\delta_h(\mathbf{x}-\mathbf{x}_0) = \frac{1}{h^2}\phi\left(\frac{x-x_0}{h}\right)\phi\left(\frac{y-y_0}{h}\right), \tag{18}$$

as kernels in a transfer step, where $\phi(r)$ is the one-dimensional (1D) discrete delta functions (r can be $(x-x_0)/h$ or $(y-y_0)/h$); and h the grid size. The relation of the velocity and force between the two types of nodes can be given by Uhlmann (2005)

$$\widetilde{\mathbf{U}}(\mathbf{X}_l^k) = \sum_{\mathbf{x}\in g_h} \widetilde{\mathbf{u}}(\mathbf{x})\delta_h(\mathbf{x}-\mathbf{X}_l^k)h^2 \quad \forall 1 \le l \le N_L,\ 1 \le k \le N_{esb}, \tag{19}$$

$$\mathbf{f}_I(\mathbf{x}) = \sum_{k=1}^{N_{esb}}\sum_{l=1}^{N_L} \mathbf{F}_I(\mathbf{X}_l^k)\delta_h(\mathbf{x}-\mathbf{X}_l^k)\Delta V_l^k \quad \forall \mathbf{x} \in g_h, \tag{20}$$

where the temporal superscript is dropped for brevity and ΔV_l^k is the volume covering the lth Lagrangian node of the kth solid body. For 2D problems, this volume is simply taken as $\Delta V_l^k = \Delta s^2$ [Uhlmann (2005)], where Δs is a Lagrangian grid size that is chosen so that $\Delta s \approx h$ (h-the Eulerian grid size).

In Peskin (2002), several axioms, including momentum conditions and a quadratic condition, are described. These axioms lead to the unique definition of a particular smoothed delta function with finite support. A family of such functions may be generated by imposing additional moment conditions and correspondingly broadening the support. The several commonly used discrete delta functions can be cited as the 2-point hat function $\delta_{2h}(r)$ [Leveque and Li (1994)], the 3-point discrete delta function $\delta_{3h}(r)$ [Roma, Peskin, and Berger (1999)] and the 4-point piecewise function $\delta_{4h}(r)$ [Peskin (2002)]. Their 1D forms are given below

$$\phi_2(r) = \begin{cases} 1-|r|, & |r| \le 1, \\ 0, & 1 \le |r|, \end{cases} \tag{21}$$

$$\phi_3(r) = \begin{cases} \frac{1}{3}\left(1+\sqrt{-3r^2+1}\right), & |r| \le 0.5, \\ \frac{1}{6}\left(5-3|r|-\sqrt{-3(1-|r|)^2+1}\right), & 0.5 \le |r| \le 1.5, \\ 0, & 1.5 \le |r|, \end{cases} \tag{22}$$

$$\phi_4(r) = \begin{cases} \frac{1}{8}\left(3-2|r|+\sqrt{1+4|r|-4r^2}\right), & |r| \le 1, \\ \frac{1}{8}\left(5-2|r|-\sqrt{-7+12|r|-4r^2}\right), & 1 \le |r| \le 2, \\ 0, & 2 \le |r|. \end{cases} \tag{23}$$

In the present study, we employ the 3-point discrete delta function $\delta_{3h}(r)$ [Roma, Peskin, and Berger (1999)].

3.2 Spatial discretisation

In this paper, the spatial derivatives are discretised using the CIRBF-2 scheme described in Thai-Quang, Mai-Duy, Tran, and Tran-Cong (2012) and modified as follows. At the boundary nodes, the compact 4-point stencils are replaced with a newly derived compact 2-point stencil in order to make the coefficient matrices tridiagonal. The present scheme is named CIRBF-3.

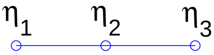

Figure 2: Compact 3-point IRBF stencil.

At an interior grid point $\mathbf{x}_{i,j} = (x_{i,j}, y_{i,j})^T$ $(i \in \{2,3,\ldots,n_x-1\}$ and $j \in \{2,3,\ldots,n_y-1\})$, its associated 3-point stencils are $[x_{i-1,j}, x_{i,j}, x_{i+1,j}]$ in the x-direction and $[y_{i,j-1}, y_{i,j}, y_{i,j+1}]$ in the y-direction. For the sake of convenience, we use η to denote x and y, thus having a generic stencil $[\eta_1, \eta_2, \eta_3]$ $(\eta_1 < \eta_2 < \eta_3,\ \eta_2 \equiv \eta_{i,j})$ as shown in Figure 2. The integral approach starts with the decomposition of the highest-order (second-order in this case) derivatives of u into RBFs

$$\frac{d^2u(\eta)}{d\eta^2} = \sum_{i=1}^{m} w_i G_i(\eta), \tag{24}$$

where $\{G_i(\eta)\}_{i=1}^{m}$ is the set of RBFs; and $\{w_i\}_{i=1}^{m}$ the set of weights/coefficients to be found. Approximate representations for the first-order derivative and the function itself are then obtained through integration

$$\frac{du(\eta)}{d\eta} = \sum_{i=1}^{m} w_i H_i(\eta) + c_1, \tag{25}$$

$$u(\eta) = \sum_{i=1}^{m} w_i \overline{H}_i(\eta) + c_1\eta + c_2, \tag{26}$$

where $H_i(\eta) = \int G_i(\eta)d\eta$; $\overline{H}_i(\eta) = \int H_i(\eta)d\eta$; and c_1 and c_2 are the constants of integration.

The value of m is taken to be 3 for interior local stencils and 2 for boundary local stencils.

3.2.1 First-order derivative compact approximations

To approximate nodal values of the first-order derivative, the conversion system of the present compact 3-node stencil is constructed as

$$\begin{pmatrix} u_1 \\ u_2 \\ u_3 \\ \frac{du_1}{d\eta} \\ \frac{du_3}{d\eta} \end{pmatrix} = \underbrace{\begin{pmatrix} \overline{\mathscr{H}} \\ \mathscr{H} \end{pmatrix}}_{\mathscr{C}_1} \begin{pmatrix} w_1 \\ w_2 \\ w_3 \\ c_1 \\ c_2 \end{pmatrix}, \tag{27}$$

where $u_i = u(\eta_i)$ $(i \in \{1,2,3\})$; $\frac{du_i}{d\eta} = \frac{du}{d\eta}(\eta_i)$ $(i \in \{1,3\})$; $\mathscr{C}_1$ is the conversion matrix and $\overline{\mathscr{H}}$, $\mathscr{H}$ are submatrices defined as

$$\overline{\mathscr{H}} = \begin{bmatrix} \overline{H}_1(\eta_1) & \overline{H}_2(\eta_1) & \overline{H}_3(\eta_1) & \eta_1 & 1 \\ \overline{H}_1(\eta_2) & \overline{H}_2(\eta_2) & \overline{H}_3(\eta_2) & \eta_2 & 1 \\ \overline{H}_1(\eta_3) & \overline{H}_2(\eta_3) & \overline{H}_3(\eta_3) & \eta_3 & 1 \end{bmatrix}, \tag{28}$$

$$\mathscr{H} = \begin{bmatrix} H_1(\eta_1) & H_2(\eta_1) & H_3(\eta_1) & 1 & 0 \\ H_1(\eta_3) & H_2(\eta_3) & H_3(\eta_3) & 1 & 0 \end{bmatrix}. \tag{29}$$

Solving (27) yields

$$\begin{pmatrix} w_1 \\ w_2 \\ w_3 \\ c_1 \\ c_2 \end{pmatrix} = \mathscr{C}_1^{-1} \begin{pmatrix} u_1 \\ u_2 \\ u_3 \\ \frac{du_1}{d\eta} \\ \frac{du_3}{d\eta} \end{pmatrix}, \tag{30}$$

which maps the vector of nodal values of the function and of its first-order derivative to the vector of RBF coefficients including the two integration constants. Approximate expression for the first-order derivative in the physical space is obtained by substituting (30) into (25)

$$\frac{du(\eta)}{d\eta} = \begin{bmatrix} H_1(\eta) & H_2(\eta) & H_3(\eta) & 1 & 0 \end{bmatrix} \mathscr{C}_1^{-1} \begin{pmatrix} \widehat{u} \\ \widehat{\frac{du}{d\eta}} \end{pmatrix}, \tag{31}$$

where $\eta_1 \leq \eta \leq \eta_3$; $\widehat{u} = (u_1, u_2, u_3)^T$; and $\widehat{\frac{du}{d\eta}} = \left(\frac{du_1}{d\eta}, \frac{du_3}{d\eta}\right)^T$. It can be rewritten in the form

$$\frac{du(\eta)}{d\eta} = \sum_{i=1}^{3} \frac{d\phi_i(\eta)}{d\eta} u_i + \frac{d\phi_4(\eta)}{d\eta}\frac{du_1}{d\eta} + \frac{d\phi_5(\eta)}{d\eta}\frac{du_3}{d\eta}, \tag{32}$$

where $\{\phi_i(\eta)\}_{i=1}^{5}$ is the set of integrated RBFs in the physical space.
At the current time level, equation (32) is taken as

$$\frac{du^n(\eta)}{d\eta} = \sum_{i=1}^{3} \frac{d\phi_i(\eta)}{d\eta} u_i^n + \frac{d\phi_4(\eta)}{d\eta}\frac{du_1^n}{d\eta} + \frac{d\phi_5(\eta)}{d\eta}\frac{du_3^n}{d\eta}, \tag{33}$$

where nodal values of the first-order derivatives on the right hand side are treated as unknowns.
Collocating (33) at the central node of the compact stencil, i.e. $\eta = \eta_2$, results in

$$-\frac{d\phi_4(\eta_2)}{d\eta}\frac{du_1^n}{d\eta} + \frac{du_2^n}{d\eta} - \frac{d\phi_5(\eta_2)}{d\eta}\frac{du_3^n}{d\eta} = \frac{d\phi_1(\eta_2)}{d\eta}u_1^n + \frac{d\phi_2(\eta_2)}{d\eta}u_2^n + \frac{d\phi_3(\eta_2)}{d\eta}u_3^n, \tag{34}$$

or in matrix-vector form

$$\begin{bmatrix} -\frac{d\phi_4(\eta_2)}{d\eta} & 1 & -\frac{d\phi_5(\eta_2)}{d\eta} \end{bmatrix} \begin{bmatrix} \frac{du_1^n}{d\eta} \\ \frac{du_2^n}{d\eta} \\ \frac{du_3^n}{d\eta} \end{bmatrix} = \begin{bmatrix} \frac{d\phi_1(\eta_2)}{d\eta} & \frac{d\phi_2(\eta_2)}{d\eta} & \frac{d\phi_3(\eta_2)}{d\eta} \end{bmatrix} \begin{bmatrix} u_1^n \\ u_2^n \\ u_3^n \end{bmatrix}. \tag{35}$$

Figure 3: Special compact 2-point IRBF stencils for the left and right boundary nodes

At the boundary nodes, we compute the first derivative here using special compact local stencils (Figure 3). These proposed stencils are constructed as follows. Consider a boundary node η_1. Its associated stencil is $[\eta_1, \eta_2]$. The conversion system of this stencil is presented as the following matrix-vector multiplication

$$\begin{pmatrix} u_1 \\ u_2 \\ \frac{du_2}{d\eta} \end{pmatrix} = \underbrace{\begin{pmatrix} \overline{\mathscr{H}_{sp}} \\ \mathscr{H}_{sp} \end{pmatrix}}_{\mathscr{C}_{sp_1}} \begin{pmatrix} w_1 \\ w_2 \\ c_1 \\ c_2 \end{pmatrix}, \tag{36}$$

where $\mathscr{C}_{sp_1}$ is the conversion matrix; and $\overline{\mathscr{H}_{sp}}$, $\mathscr{H}_{sp}$ matrices defined as

$$\overline{\mathscr{H}_{sp}}=\begin{bmatrix} \overline{H}_1(\eta_1) & \overline{H}_2(\eta_1) & \eta_1 & 1 \\ \overline{H}_1(\eta_2) & \overline{H}_2(\eta_2) & \eta_2 & 1 \end{bmatrix}, \tag{37}$$

$$\mathscr{H}_{sp}=\begin{bmatrix} H_1(\eta_2) & H_2(\eta_2) & 1 & 0 \end{bmatrix}. \tag{38}$$

Solving (36) yields

$$\begin{pmatrix} w_1 \\ w_2 \\ c_1 \\ c_2 \end{pmatrix}=\mathscr{C}_{sp_1}^{-1}\begin{pmatrix} u_1 \\ u_2 \\ \frac{du_2}{d\eta} \end{pmatrix}. \tag{39}$$

The boundary value of the first-order derivative of u is thus obtained by substituting (39) into (25) and taking $\eta=\eta_1$

$$\frac{du(\eta_1)}{d\eta}=\begin{bmatrix} H_1(\eta_1) & H_2(\eta_1) & 1 & 0 \end{bmatrix}\mathscr{C}_{sp_1}^{-1}\begin{pmatrix} u_1 & u_2 & \frac{du_2}{d\eta} \end{pmatrix}^T, \tag{40}$$

or

$$\frac{du_1^n}{d\eta}-\frac{d\phi_{sp_3}(\eta_1)}{d\eta}\frac{du_2^n}{d\eta}=\frac{d\phi_{sp_1}(\eta_1)}{d\eta}u_1^n+\frac{d\phi_{sp_2}(\eta_1)}{d\eta}u_2^n, \tag{41}$$

where $\{\phi_{sp_i}(\eta)\}_{i=1}^3$ is the set of IRBFs in the physical space. We rewrite equation (41) in matrix-vector form

$$\begin{bmatrix} 1 & -\frac{d\phi_{sp_3}(\eta_1)}{d\eta} \end{bmatrix}\begin{bmatrix} \frac{du_1^n}{d\eta} \\ \frac{du_2^n}{d\eta} \end{bmatrix}=\begin{bmatrix} \frac{d\phi_{sp_1}(\eta_1)}{d\eta} & \frac{d\phi_{sp_2}(\eta_1)}{d\eta} \end{bmatrix}\begin{bmatrix} u_1^n \\ u_2^n \end{bmatrix}. \tag{42}$$

In a similar manner, one can calculate the first derivative of u at the other boundary node η_{n_η}.

The IRBF system on a grid line for the first derivative of u is obtained by letting the interior node taking value from 2 to $(n_\eta-1)$ in (35) and making use of (42),

$$\mathscr{L}_\eta\widehat{u}_\eta^n=\mathscr{A}_\eta\widehat{u}^n. \tag{43}$$

3.2.2 Second-order derivative compact approximations

To approximate nodal values of the second-order derivative, we represent the conversion system of the present compact stencil as a matrix-vector multiplication

$$\begin{pmatrix} u_1 \\ u_2 \\ u_3 \\ \frac{d^2u_1}{d\eta^2} \\ \frac{d^2u_3}{d\eta^2} \end{pmatrix}=\underbrace{\begin{pmatrix} \overline{\mathscr{H}} \\ \mathscr{G} \end{pmatrix}}_{\mathscr{C}_2}\begin{pmatrix} w_1' \\ w_2' \\ w_3' \\ c_1' \\ c_2' \end{pmatrix}, \tag{44}$$

where $u_i = u(\eta_i)$ $(i \in \{1,2,3\})$; $\frac{d^2u_i}{d\eta^2} = \frac{d^2u}{d\eta^2}(\eta_i)$ $(i \in \{1,3\})$; $\mathscr{C}_2$ the conversion matrix; and $\overline{\mathscr{H}}$, $\mathscr{G}$ submatrices defined as (28) and

$$\mathscr{G} = \begin{bmatrix} G_1(\eta_1) & G_2(\eta_1) & G_3(\eta_1) & 0 & 0 \\ G_1(\eta_3) & G_2(\eta_3) & G_3(\eta_3) & 0 & 0 \end{bmatrix}, \text{ respectively.} \tag{45}$$

Solving (44) yields

$$\begin{pmatrix} w'_1 \\ w'_2 \\ w'_3 \\ c'_1 \\ c'_2 \end{pmatrix} = \mathscr{C}_2^{-1} \begin{pmatrix} u_1 \\ u_2 \\ u_3 \\ \frac{d^2u_1}{d\eta^2} \\ \frac{d^2u_3}{d\eta^2} \end{pmatrix}, \tag{46}$$

which maps the vector of nodal values of the function and of its second-order derivative to the vector of RBF coefficients including the two integration constants. Approximate expression for the second-order derivative in the physical space is obtained by substituting (46) into (24)

$$\frac{d^2u(\eta)}{d\eta^2} = \begin{bmatrix} G_1(\eta) & G_2(\eta) & G_3(\eta) & 0 & 0 \end{bmatrix} \mathscr{C}_2^{-1} \begin{pmatrix} \widehat{u} \\ \widehat{\frac{d^2u}{d\eta^2}} \end{pmatrix}, \tag{47}$$

where $\eta_1 \le \eta \le \eta_3$; $\widehat{u} = (u_1, u_2, u_3)^T$; and $\widehat{\frac{d^2u}{d\eta^2}} = \left(\frac{d^2u_1}{d\eta^2}, \frac{d^2u_3}{d\eta^2}\right)^T$. It can be rewritten in the form

$$\frac{d^2u(\eta)}{d\eta^2} = \sum_{i=1}^{3} \frac{d^2\varphi_i(\eta)}{d\eta^2} u_i + \frac{d^2\varphi_4(\eta)}{d\eta^2}\frac{d^2u_1}{d\eta^2} + \frac{d^2\varphi_5(\eta)}{d\eta^2}\frac{d^2u_3}{d\eta^2}, \tag{48}$$

or

$$\frac{d^2u^n(\eta)}{d\eta^2} = \sum_{i=1}^{3} \frac{d^2\varphi_i(\eta)}{d\eta^2} u_i^n + \frac{d^2\varphi_4(\eta)}{d\eta^2}\frac{d^2u_1^n}{d\eta^2} + \frac{d^2\varphi_5(\eta)}{d\eta^2}\frac{d^2u_3^n}{d\eta^2}, \tag{49}$$

where $\{\varphi_i(\eta)\}_{i=1}^5$ is the set of IRBFs in the physical space.

Collocating (49) at the central node of the compact stencil, i.e. $\eta = \eta_2$, leads to

$$-\frac{d^2\varphi_4(\eta_2)}{d\eta^2}\frac{d^2u_1^n}{d\eta^2} + \frac{d^2u_2^n}{d\eta^2} - \frac{d^2\varphi_5(\eta_2)}{d\eta^2}\frac{d^2u_3^n}{d\eta^2} = \frac{d^2\varphi_1(\eta_2)}{d\eta^2}u_1^n + \frac{d^2\varphi_2(\eta_2)}{d\eta^2}u_2^n + \frac{d^2\varphi_3(\eta_2)}{d\eta^2}u_3^n, \tag{50}$$

or in matrix-vector form

$$\begin{bmatrix} -\frac{d^2\varphi_4(\eta_2)}{d\eta^2} & 1 & -\frac{d^2\varphi_5(\eta_2)}{d\eta^2} \end{bmatrix} \begin{bmatrix} \frac{d^2u_1^n}{d\eta^2} \\ \frac{d^2u_2^n}{d\eta^2} \\ \frac{d^2u_3^n}{d\eta^2} \end{bmatrix} = \begin{bmatrix} \frac{d^2\varphi_1(\eta_2)}{d\eta^2} & \frac{d^2\varphi_2(\eta_2)}{d\eta^2} & \frac{d^2\varphi_3(\eta_2)}{d\eta^2} \end{bmatrix} \begin{bmatrix} u_1^n \\ u_2^n \\ u_3^n \end{bmatrix}. \tag{51}$$

At the boundary nodes, we compute the second derivative here using special compact local stencils (Figure 3). Consider a boundary node, e.g., η_1. The conversion system of its associated 2-node stencil is presented as the following matrix-vector multiplication

$$\begin{pmatrix} u_1 \\ u_2 \\ \frac{d^2u_2}{d\eta^2} \end{pmatrix} = \underbrace{\begin{pmatrix} \overline{\mathscr{H}_{sp}} \\ \mathscr{G}_{sp} \end{pmatrix}}_{\mathscr{C}_{sp_2}} \begin{pmatrix} w_1 \\ w_2 \\ c_1 \\ c_2 \end{pmatrix}, \tag{52}$$

where $\mathscr{C}_{sp_2}$ is the conversion matrix; $\overline{\mathscr{H}_{sp}}$ defined as before; and

$$\mathscr{G}_{sp} = \begin{bmatrix} G_1(\eta_2) & G_2(\eta_2) & 0 & 0 \end{bmatrix}. \tag{53}$$

Solving (52) yields

$$\begin{pmatrix} w_1 \\ w_2 \\ c_1 \\ c_2 \end{pmatrix} = \mathscr{C}_{sp_2}^{-1} \begin{pmatrix} u_1 \\ u_2 \\ \frac{d^2u_2}{d\eta^2} \end{pmatrix}. \tag{54}$$

The boundary value of the second-order derivative of u is thus obtained by substituting (54) into (24) and taking $\eta = \eta_1$

$$\frac{d^2u(\eta_1)}{d\eta^2} = \begin{bmatrix} G_1(\eta_1) & G_2(\eta_1) & 0 & 0 \end{bmatrix} \mathscr{C}_{sp_2}^{-1} \begin{pmatrix} u_1 & u_2 & \frac{d^2u_2}{d\eta^2} \end{pmatrix}^T, \tag{55}$$

or

$$\frac{d^2u_1^n}{d\eta^2} - \frac{d^2\varphi_{sp_3}(\eta_1)}{d\eta^2}\frac{d^2u_2^n}{d\eta^2} = \frac{d^2\varphi_{sp_1}(\eta_1)}{d\eta^2}u_1^n + \frac{d^2\varphi_{sp_2}(\eta_1)}{d\eta^2}u_2^n, \tag{56}$$

where $\{\varphi_{sp_i}(\eta)\}_{i=1}^3$ is the set of IRBFs in the physical space. We rewrite equation (56) in matrix-vector form

$$\begin{bmatrix} 1 & -\frac{d^2\varphi_{sp_3}(\eta_1)}{d\eta^2} \end{bmatrix} \begin{bmatrix} \frac{d^2u_1^n}{d\eta^2} \\ \frac{d^2u_2^n}{d\eta^2} \end{bmatrix} = \begin{bmatrix} \frac{d^2\varphi_{sp_1}(\eta_1)}{d\eta^2} & \frac{d^2\varphi_{sp_2}(\eta_1)}{d\eta^2} \end{bmatrix} \begin{bmatrix} u_1^n \\ u_2^n \end{bmatrix}. \tag{57}$$

The IRBF system on a grid line for the second derivative of u is obtained by letting the interior node taking value from 2 to $(n_\eta - 1)$ in (51) and making use of (57),

$$\mathscr{L}_{\eta\eta}\widehat{u}^n_{\eta\eta} = \mathscr{B}_{\eta\eta}\widehat{u}^n, \tag{58}$$

where $\mathscr{L}_{\eta\eta}$, $\mathscr{B}_{\eta\eta}$ are $n_\eta \times n_\eta$ matrices.

3.3 Temporal discretisation

The temporal discretisation of (1)-(3) using the Adams-Bashforth scheme [Butcher (2003)] for the convection term and the Crank-Nicolson scheme [Crank and Nicolson (1996)] for the diffusion term yields

$$\nabla.\mathbf{u}^n = 0, \tag{59}$$

$$\frac{\mathbf{u}^n - \mathbf{u}^{n-1}}{\Delta t} + \left[\frac{3}{2}(\mathbf{u}^{n-1}.\nabla)\mathbf{u}^{n-1} - \frac{1}{2}(\mathbf{u}^{n-2}.\nabla)\mathbf{u}^{n-2}\right] = \\ -\nabla p^{n-1/2} + \frac{1}{2}\sqrt{\frac{Pr}{Ra}}\left(\nabla^2\mathbf{u}^n + \nabla^2\mathbf{u}^{n-1}\right) + \mathbf{f}_b^{n-1/2} + \mathbf{f}_I^{n-1/2}, \tag{60}$$

$$\frac{T^n - T^{n-1}}{\Delta t} + \left[\frac{3}{2}(\mathbf{u}^{n-1}.\nabla)T^{n-1} - \frac{1}{2}(\mathbf{u}^{n-2}.\nabla)T^{n-2}\right] = \\ \frac{1}{2\sqrt{PrRa}}\left(\nabla^2 T^n + \nabla^2 T^{n-1}\right) + f_{I,T}^{n-1/2}. \tag{61}$$

We apply the pressure-free projection/fractional-step method developed in Kim and Moin (1985) to solve (60). This equation is advanced in time according to the following two step procedure

$$\frac{\mathbf{u}^{*,n} - \mathbf{u}^{n-1}}{\Delta t} + \left[\frac{3}{2}(\mathbf{u}^{n-1}.\nabla)\mathbf{u}^{n-1} - \frac{1}{2}(\mathbf{u}^{n-2}.\nabla)\mathbf{u}^{n-2}\right] = \\ \frac{1}{2}\sqrt{\frac{Pr}{Ra}}\left(\nabla^2\mathbf{u}^{*,n} + \nabla^2\mathbf{u}^{n-1}\right) + \mathbf{f}_b^{n-1/2} + \mathbf{f}_I^{n-1/2}, \tag{62}$$

$$\frac{\mathbf{u}^n - \mathbf{u}^{*,n}}{\Delta t} = -\nabla\phi^n, \tag{63}$$

where $\mathbf{u}^* = (u^*, v^*)^T$ denotes the intermediate velocity vector; and ϕ the pseudo-pressure. It is noted that $\mathbf{u}^{*,n}$ does not satisfy the continuity equation (59) and the actual pressure p is derived as

$$p^{n-1/2} = \phi^n - \left(\frac{\Delta t}{2}\sqrt{\frac{Pr}{Ra}}\right)\nabla^2\phi^n. \tag{64}$$

3.4 Algorithm of the computational procedure

- Step 0: Start with the given initial and boundary conditions. In this study, the initial conditions are zero for the velocity and temperature fields.

- Step 1: Compute thermal Eulerian counterpart $\widetilde{\mathbf{t}}^n$, using a formula similar to (15), which is then transferred to Lagrangian nodes to obtain $\widetilde{\mathbf{T}}^n$ using a formula similar to (19).

- Step 2: Compute $F_{I,T}^{n-1/2}$, using a formula similar to (17), which is then transferred to Eulerian nodes to obtain $f_{I,T}^{n-1/2}$ using a formula similar to (20).

- Step 3: Solve (61) for the solution T^n with known $f_{I,T}^{n-1/2}$ and prescribed boundary condition T_Γ^n.

- Step 4: Compute the body force $\mathbf{f}_b^{n-1/2}$ from the temperature field as

$$\mathbf{f}_b^{n-1/2} = \left(0, T^{n-1/2}\right)^T = \left(0, \frac{T^n + T^{n-1}}{2}\right)^T. \tag{65}$$

- Step 5: Compute momentum Eulerian counterpart $\widetilde{\mathbf{u}}^n$ from (15), which is then transferred to Lagrangian nodes to obtain $\widetilde{\mathbf{U}}^n$ via (19).

- Step 6: Compute $\mathbf{F}_I^{n-1/2}$ from (17), which is then transferred to Eulerian nodes to obtain $\mathbf{f}_I^{n-1/2}$ via (20).

- Step 7: Solve (62) for $\mathbf{u}^{*,n}$ subject to the following boundary condition [Kim and Moin (1985)]

$$\mathbf{u}^{*,n}|_\Gamma = \mathbf{u}_b^n + \Delta t \left(\nabla \phi^{n-1}\right)|_\Gamma. \tag{66}$$

  For a more efficient solution, one can apply the alternating direction implicit (ADI) algorithm to solve (62) and (61) as shown in Thai-Quang, Mai-Duy, Tran, and Tran-Cong (2012).

- Step 8: Equations (63) and (59) are then solved in a coupled manner for $\mathbf{u}^n$ and ϕ^n in which the boundary condition for the pseudo-pressure ϕ is not required. The values of ϕ^n are obtained for the interior nodes only. After that, the values of ϕ at the boundary nodes are extrapolated from known values at the interior nodes and known Neumann boundary values derived from (63) (i.e., $\nabla\phi^n|_\Gamma = \left(\mathbf{u}_b^{*,n} - \mathbf{u}_b^n\right)/\Delta t$) [Thai-Quang, Le-Cao, Mai-Duy, and Tran-Cong (2012)]:

$$\begin{pmatrix}\phi^n_{1,j}\\ \phi^n_{nx,j}\end{pmatrix} = \begin{bmatrix}\overline{H}_1(x_{1,j}) & \cdots & \overline{H}_{n_x}(x_{1,j}) & x_{1,j} & 1\\ \overline{H}_1(x_{n_x,j}) & \cdots & \overline{H}_{n_x}(x_{n_x,j}) & x_{n_x,j} & 1\end{bmatrix}$$

$$\begin{bmatrix}\overline{H}_1(x_{2,j}) & \cdots & \overline{H}_{n_x}(x_{2,j}) & x_{2,j} & 1\\ \overline{H}_1(x_{3,j}) & \cdots & \overline{H}_{n_x}(x_{3,j}) & x_{3,j} & 1\\ \vdots & \ddots & \vdots & \vdots & \vdots\\ \overline{H}_1(x_{n_x-1,j}) & \cdots & \overline{H}_{n_x}(x_{n_x-1,j}) & x_{n_x-1,j} & 1\\ H_1(x_{1,j}) & \cdots & H_{n_x}(x_{1,j}) & 1 & 0\\ H_1(x_{n_x,j}) & \cdots & H_{n_x}(x_{n_x,j}) & 1 & 0\end{bmatrix}^{-1}\begin{pmatrix}\phi^n_{2,j}\\ \phi^n_{3,j}\\ \vdots\\ \phi^n_{n_x-1,j}\\ \partial\phi^n_{1,j}/\partial x\\ \partial\phi^n_{n_x,j}/\partial x\end{pmatrix}, \tag{67}$$

for a x-grid line, and

$$\begin{pmatrix}\phi^n_{i,1}\\ \phi^n_{i,n_y}\end{pmatrix} = \begin{bmatrix}\overline{H}_1(y_{i,1}) & \cdots & \overline{H}_{n_y}(y_{i,1}) & y_{i,1} & 1\\ \overline{H}_1(y_{i,n_y}) & \cdots & \overline{H}_{n_y}(y_{i,n_y}) & y_{i,n_y} & 1\end{bmatrix}$$

$$\begin{bmatrix}\overline{H}_1(y_{i,2}) & \cdots & \overline{H}_{n_y}(y_{i,2}) & y_{i,2} & 1\\ \overline{H}_1(y_{i,3}) & \cdots & \overline{H}_{n_y}(y_{i,3}) & y_{i,3} & 1\\ \vdots & \ddots & \vdots & \vdots & \vdots\\ \overline{H}_1(y_{i,n_y-1}) & \cdots & \overline{H}_{n_y}(y_{i,n_y-1}) & y_{i,n_y-1} & 1\\ H_1(y_{i,1}) & \cdots & H_{n_y}(y_{i,1}) & 1 & 0\\ H_1(y_{i,n_y}) & \cdots & H_{n_y}(y_{i,n_y}) & 1 & 0\end{bmatrix}^{-1}\begin{pmatrix}\phi^n_{i,2}\\ \phi^n_{i,3}\\ \vdots\\ \phi^n_{i,n_y-1}\\ \partial\phi^n_{i,1}/\partial y\\ \partial\phi^n_{i,n_y}/\partial y\end{pmatrix}, \tag{68}$$

for a y-grid line. It is noted that for flows with irregular outer boundaries, instead of solving (63) and (59), we solve (59)-(60) simultaneously for $\mathbf{u}^n$ and $p^{n-1/2}$ in which $p^{n-1/2}$ involves the interior nodes only (the boundary condition for $p^{n-1/2}$ is not required here).

- Step 9: Go back to step 1 and iterate for the next time level.

4 Numerical examples

It has generally been accepted that, among RBFs, the multiquadric (MQ) function tends to result in the most accurate approximation [Franke (1982)]. We choose MQ as the basis function in the present calculations

$$G_i(\mathbf{x}) = \sqrt{(\mathbf{x}-\mathbf{c}_i)^T(\mathbf{x}-\mathbf{c}_i)+a_i^2}, \tag{69}$$

where $\mathbf{x} = (x,y)^T$ is the position vector of the point of interest; and $\mathbf{c}_i = (x_{c_i}, y_{c_i})^T$ and a_i the position vector of the centre and the width of the ith MQ, respectively.

For each stencil, the set of nodal points is taken to be the set of MQ centres. We simply choose the MQ width as $a_i = \beta h_i$ in which β is a given positive number and h_i the distance between the ith node and its nearest neighbouring node. For the calculations in this paper, $\beta = 25$ and $\beta = 50$ are employed. We assess the performance of the present scheme through following measures:

- the root mean square (RMS) error defined as

$$RMS = \sqrt{\frac{\sum_{i=1}^{N}(u_i - \bar{u}_i)^2}{N}}, \tag{70}$$

  where N is the number of nodes over the whole domain; and $\bar{u}$ the analytic solution,

- maximum absolute error (L_∞) defined as

$$L_\infty = \max_i |u_i - \bar{u}_i|, \tag{71}$$

- the error behaviour, expressed as $O(h^\alpha)$, where h is an average grid size; and α the average rate of grid convergence, determined in the least square sense,

- the convergence measure based on the velocity magnitude (CM_{vel}) in the whole analysis domain is defined as (given two successive grids)

$$CM_{vel} = \frac{\sqrt{\sum_{i=1}^{N}\left(vel_i^{ctfg} - vel_i^{fg}\right)^2}}{\sqrt{\sum_{i=1}^{N}\left(vel_i^{fg}\right)^2}}, \tag{72}$$

  where vel^{fg} is the velocity magnitude field computed using the finer grid; vel^{ctfg} is the velocity magnitude field obtained at the finer grid by interpolating the solution computed using the coarser grid. The present results is considered to be grid convergent if CM_{vel} is less than 10^{-3}.

A flow is considered to reach a steady state when

$$\sqrt{\frac{\sum_{i=1}^{N}(u_i^n - u_i^{n-1})^2}{N}} < 10^{-9}, \tag{73}$$

where u^n and u^{n-1} are the approximate solutions at the current and previous time levels, respectively.

Since the approximations are presently based on RBFs, distances between two neighbouring nodes in the stencil can be different. This capability is exploited here to handle non-rectangular outer boundaries in a direct manner (i.e. body-fitted grid). We can thus retain a body-conforming treatment for rectangular and non-rectangular outer boundaries. We numerically demonstrate this ability with the following example

$$\frac{\partial^2 u}{\partial x^2} + \frac{\partial^2 u}{\partial y^2} = -8\pi^2 \sin(2\pi x)\sin(2\pi y), \tag{74}$$

defined on a circular domain of radius $R = 1.5$ and subject to Dirichlet boundary condition. Its exact solution is $\overline{u} = \sin(2\pi x)\sin(2\pi y)$. A number of grids, namely $\{12\times 12,\ 22\times 22,\ldots,\ 102\times 102\}$, are employed to study the grid-convergence behaviour of the solution (Figure 4). Those interior nodes that fall very close to the boundary (within a distance of $h/8$) are removed from the set of of nodal points. Figure 5 shows the matrix condition number and the *RMS* error of the interior solution against grid size. Results by the Cartesian-grid finite-difference method (FDM) [Sanmiguel-Rojas, Ortega-Casanova, del Pino, and Fernandez-Feria (2005)] are also included for comparison purposes. The solution converges as $O(h^{2.03})$ for FDM and quite fast as $O(h^{3.17})$ for the present method. The two methods have similar condition numbers of the system matrix.

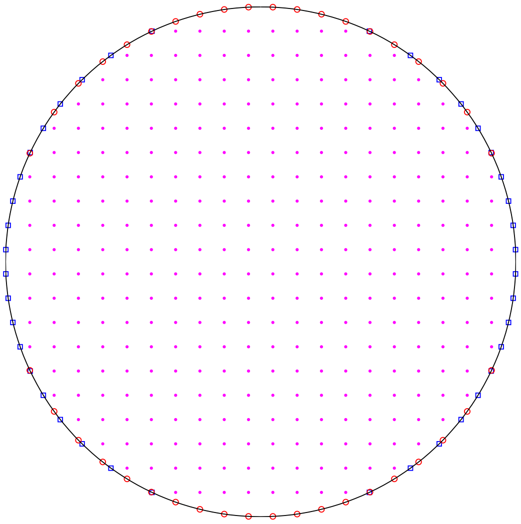

Figure 4: Poisson equation, circular domain: Computational domain and its discretisation.

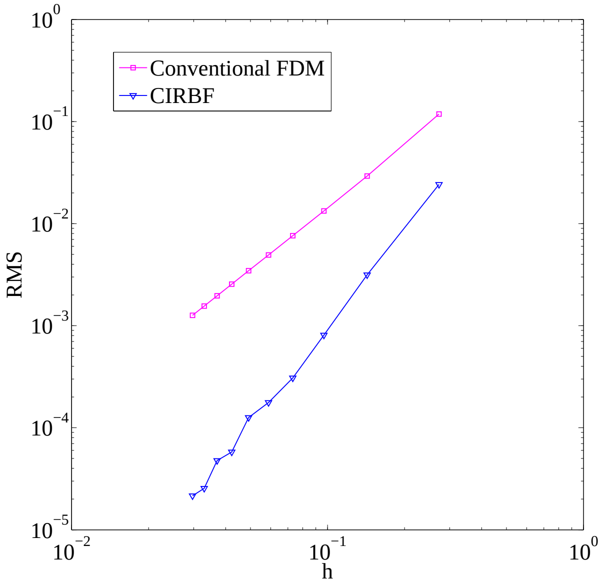

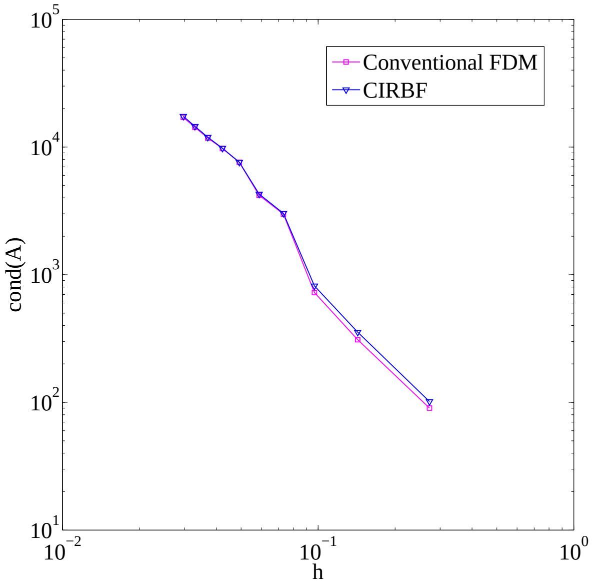

Figure 5: Poisson equation, circular domain, $\{12 \times 12, 22 \times 22, \ldots, 102 \times 102\}$: The solution accuracy (top) and the matrix condition number (bottom) against grid size by FDM and the present method. The solution converges as $O(h^{2.03})$ and $O(h^{3.17})$ while the matrix condition grows as $O(h^{-2.52})$ and $O(h^{-2.46})$ for FDM and the present method, respectively.

4.1 Taylor-Green vortices

This problem is taken from Uhlmann (2005), where the analytic solution is given by

$$\overline{u}(x,y,t) = \sin(\pi x)\cos(\pi y)e^{-2\pi^2 t/Re}, \tag{75}$$

$$\overline{v}(x,y,t) = -\sin(\pi y)\cos(\pi x)e^{-2\pi^2 t/Re}, \tag{76}$$

$$\overline{p}(x,y,t) = 0.5\left(\cos^2(\pi y) - \sin^2(\pi x)\right)e^{-4\pi^2 t/Re}, \tag{77}$$

from which one can derive the initial solution, the time-dependent boundary conditions and the time-dependent desired velocities $\mathbf{U}^{(d)}$ on the inner immersed boundaries. The solution is computed at $Re = 5$ and $t = 0.3$ using a time step $\Delta t = 0.001$ and $\beta = 25$ for the following two domains

4.1.1 Circular domain

A circular domain of unit radius is chosen here to investigate the performance of the present scheme in dealing with non-rectangular outer boundaries. Several grids, namely $\{12\times 12,\ 22\times 22, \ldots,\ 52\times 52\}$ are employed. Figure 6 shows the *RMS* errors of the velocity components and the pressure against the grid size h. The solutions converge as $O(h^{3.31})$, $O(h^{3.29})$ and $O(h^{2.87})$ for the x-component velocity, y-component velocity and pressure, respectively. It can be seen that fast rates of convergence (about third order) are achieved with the present method. Figure 7 shows the analytic and computed vorticity isolines using a grid of 52×52, which are graphically indistinguishable.

4.1.2 Concentric annulus between two circular cylinders

The outer and inner radii of this domain are taken as $R_o = 1$ and $R_i = 0.5$, respectively. We employ a set of grids, namely $\{22\times 22,\ 32\times 32, \ldots,\ 52\times 52\}$ to represent the problem domain. Figure 8 shows the Eulerian nodes distributed inside and on the outer boundary, and Lagrangian nodes distributed on the inner boundary, for instance, by a grid of 22×22. Figure 9 shows the analytic and computed vorticity isolines using a grid of 52×52, where an excellent agreement can be seen. The L_∞ errors of the velocity components and pressure against the grid size h are presented in Figure 10. The solutions converge as $O(h^{2.02})$, $O(h^{2.03})$ and $O(h^{2.02})$ for u, v and p, respectively. The rates of convergence are reduced due to the effect of using regularised δ_h functions, which are second-order accurate [Uhlmann (2005)], in the IB approach.

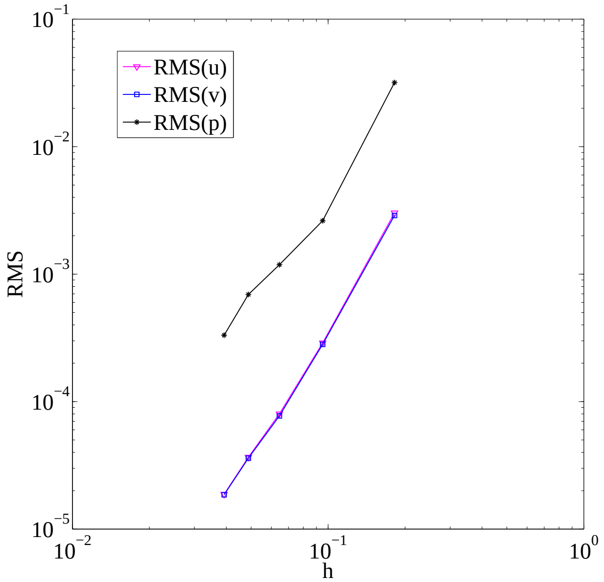

Figure 6: Taylor-Green vortices, circular domain, $\{12\times12, 22\times22, \ldots, 52\times52\}$: The solution accuracy of the velocity components and pressure against grid size. The solution converges as $O(h^{3.31})$, $O(h^{3.29})$ and $O(h^{2.87})$ for x-component velocity, y-component velocity and pressure, respectively.

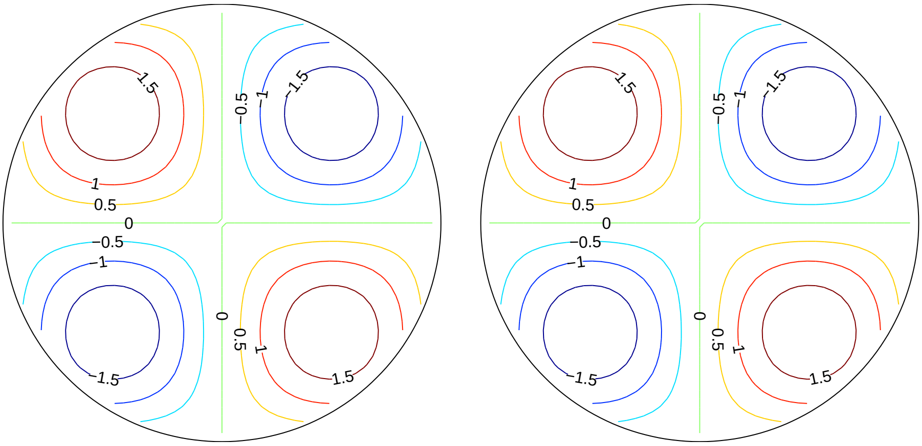

Figure 7: Taylor-Green vortices, circular domain, 52×52, $\Delta t = 0.001$: the analytic (left) and computed (right) isolines of the vorticity field at $t = 0.3$.

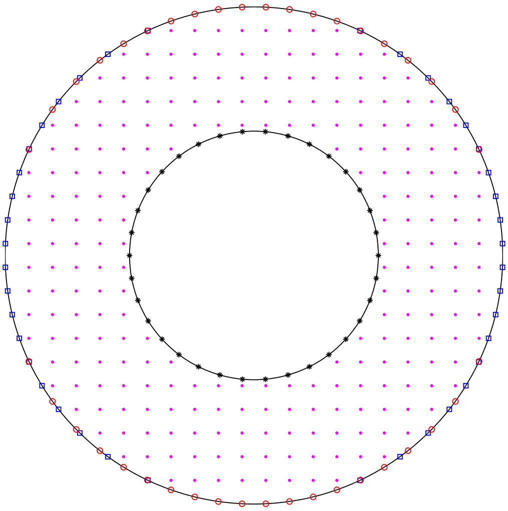

Figure 8: Taylor-Green vortices, concentric annulus: Computational domain and its discretisation (Eulerian nodes inside the annulus and on the outer boundary, Lagrangian nodes on the inner boundary with a grid of 22×22).

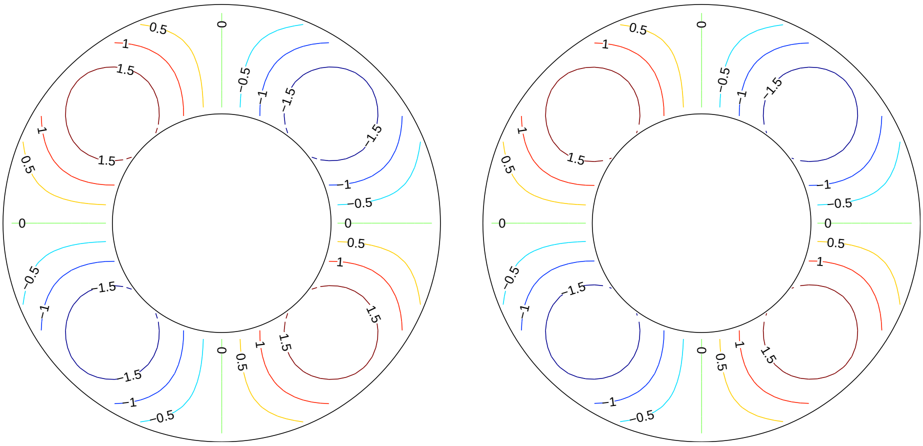

Figure 9: Taylor-Green vortices, concentric annulus, 52×52, $\Delta t = 0.001$: the analytic (left) and computed (right) isolines of the vorticity field at $t = 0.3$.

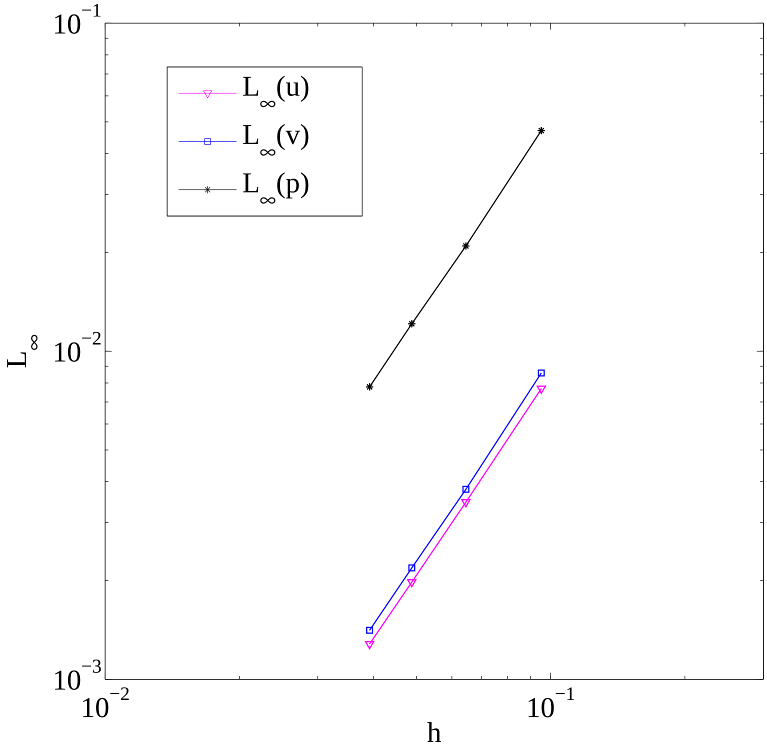

Figure 10: Taylor-Green vortices, concentric annulus, $\{22\times22, 32\times32, \ldots, 52\times52\}$: The solution accuracy of the velocity components and pressure against grid size. The solution converges as $O(h^{2.02})$, $O(h^{2.03})$ and $O(h^{2.02})$ for x-component velocity, y-component velocity and pressure, respectively.

4.2 Rotational flow

The present scheme is further verified with a rotational flow, where a circular ring (zero thickness) of $R = 0.3$ is embedded in a square domain $\Omega = [-1,1]\times[-1,1]$. The solid ring rotates about its centre with an angular velocity $\omega = 2$. The simulation is conducted for $Re = 18$ using a grid of 65×65 and $\Delta t = h/4$ as in Le, Khoo, and Peraire (2006). Plots of the velocity u and velocity vector in a subdomain $[-0.5,0.5]\times[-0.5,0.5]$ at $t = 10$ are shown in Figure 11, in which the flow behaviours observed here are very similar to those reported in Le, Khoo, and Peraire (2006).

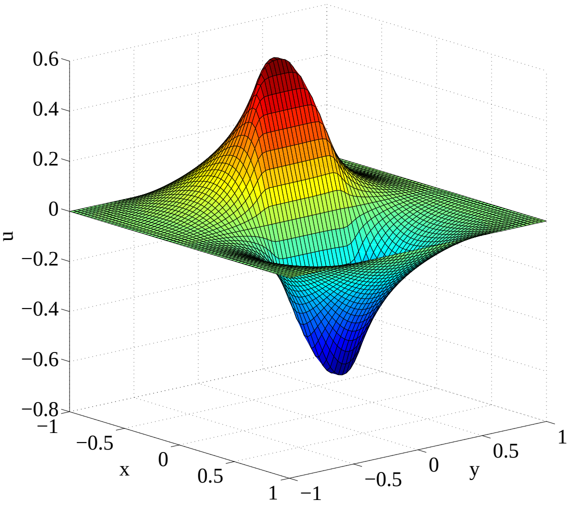

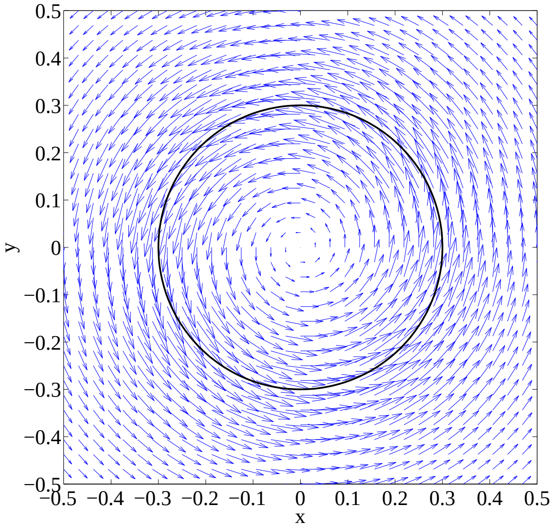

Figure 11: Rotational flow generated by a circular ring rotating about its centre in a fluid filled square cavity, $Re = 18$, 65×65, $t = 10$, $\Delta t = h/4$: Distributions of the x-component velocity (top) and velocity vector (bottom) over the computational domain.

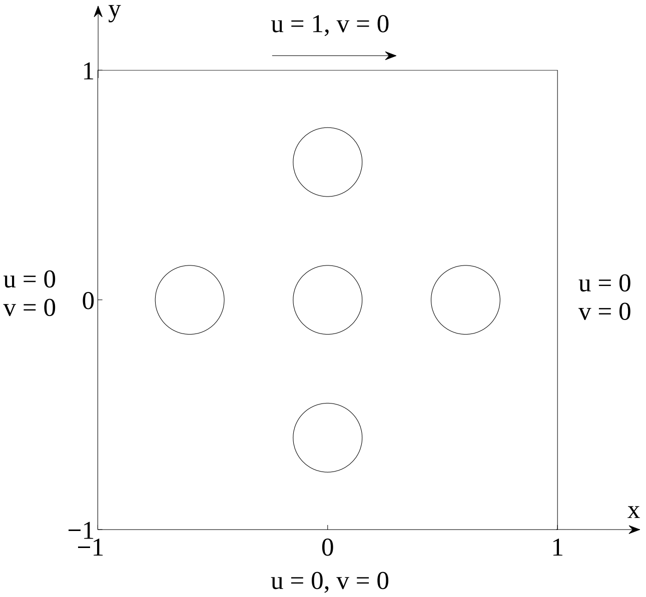

Figure 12: Lid-driven cavity flow with multiple solid bodies: Geometry and boundary condition.

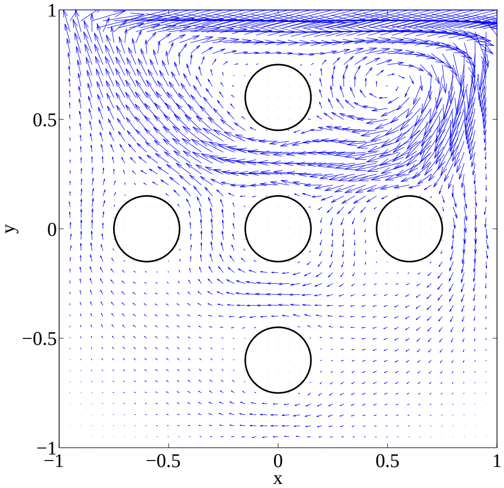

Figure 13: Lid-driven cavity flow with multiple solid bodies: Velocity vector field.

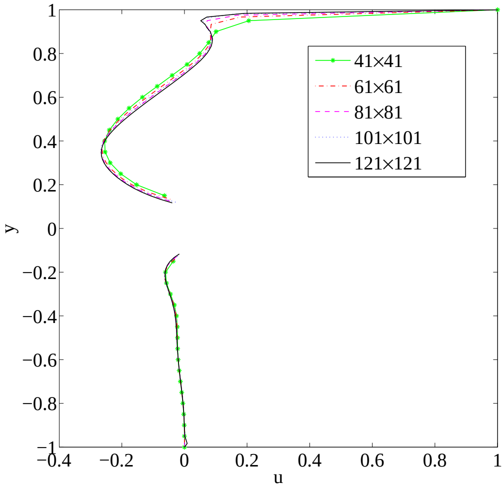

Figure 14: Lid-driven cavity flow with multiple solid bodies: The effect of the grid size on the u-velocity profile along the diagonal $x = y$. The curves are discontinuous due to the presence of a circular body on the diagonal around $x = y = 0$.

4.3 Lid-driven cavity flow with multiple solid bodies

This test problem is concerned with the lid-driven cavity flow in a square domain $\Omega = [-1,1] \times [-1,1]$ containing five fixed rigid circular cylinders (Figure 12). The radius of the cylinders is $R = 0.15$ and their centres are located at $(0,0)$, $(0,-0.6)$, $(-0.6,0)$, $(0,0.6)$ and $(0.6,0)$, respectively. The top wall is driven from left to right by a unit velocity whereas the other walls are stationary. The Lagrangian nodes are distributed on the boundaries with a grid spacing ratio $\Delta s/h = 0.85$. These parameters are taken from Su and Lai (2007).

The grid convergence study for this problem is carried out at $Re = 100$ on a set of uniform grids, namely $\{41\times41, 61\times61, 81\times81, 101\times101, 121\times121, 141\times141\}$, using a time step of $\Delta t = 0.001$. The present solutions converge at the grid of 121×121. The velocity field obtained with the grid 121×121 is presented in Figure 13, showing that the primary vortex is captured very well around the top-right corner. The flow field looks feasible and similar in comparison with those shown in Su and Lai (2007). (To avoid cluttering, the velocity vectors are plotted at every third grid point, i.e. at 41×41 points as in Su and Lai (2007)). Figure 14 shows the u-velocity profile along the diagonal $x = y$ for different grid sizes.

4.4 Flow between a rotating circular and a fixed square cylinder

Consider a flow in a concentric annulus between a square cylinder $\Omega = [-2,2] \times [-2,2]$ and a circular cylinder of $R = 1$ (Figure 15). The inner cylinder rotates with an angular velocity $\omega = 1$ while the outer cylinder is stationary. This problem is taken from Lewis (1979). The boundary conditions are as follows

$$\mathbf{u} = 0 \quad \text{on} \quad x = \pm 2,\ y = \pm 2, \tag{78}$$

$$u = -\omega y,\ v = \omega x \quad \text{on} \quad R = 1. \tag{79}$$

The calculations are carried out on a set of uniform grid $N \in \{61\times 61, 81\times 81, 101\times 101, 121\times 121, 131\times 131, 141\times 141\}$ and a set of time step $\Delta t \in \{0.001, 0.0005, 0.00025, 0.0001\}$ for various values of the Reynolds number, namely $Re \in \{1, 100, 200, 500, 1000, 1400\}$. Smaller time step is utilised for denser grid and higher Reynolds number. The maximum values of the stream function and vorticity (ψ_{max} and ζ_{max}), the values of the stream function on the circular cylinder (ψ_c) and minimum values of the stream function (ψ_{min}) are presented in Table 1. The present results, convergent at a grid of 131 × 131, agree well with those reported in Lewis (1979) using a 161 × 161 grid.

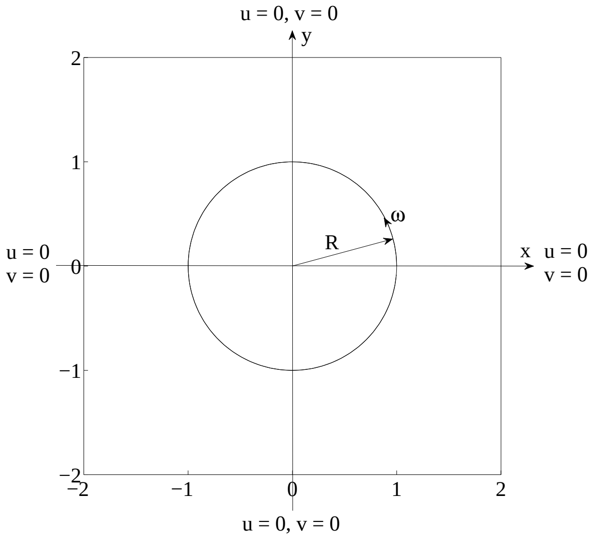

Figure 15: Flow between a rotating circular and a fixed square cylinder: Geometry and boundary conditions.

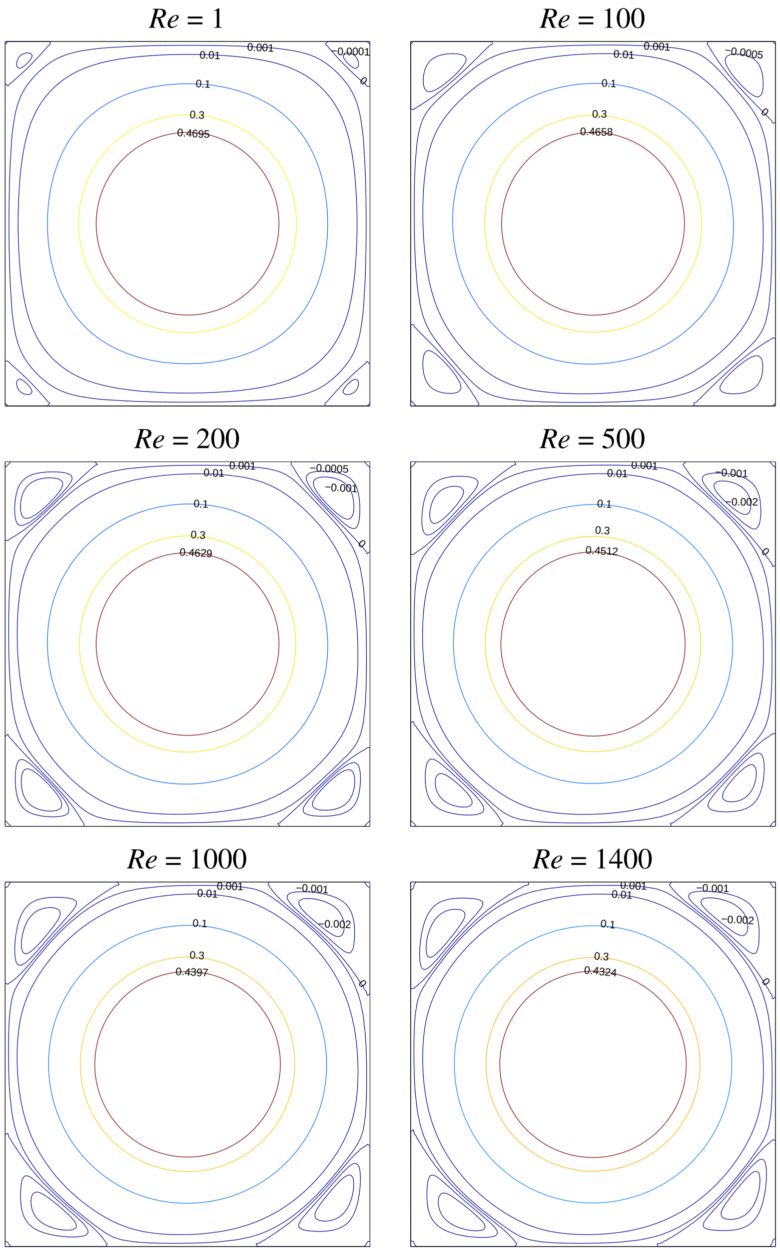
$Re = 1$ $Re = 100$ $Re = 200$ $Re = 500$ $Re = 1000$ $Re = 1400$

Figure 16: Flow between a rotating circular and a fixed square cylinder: Streamlines of the flow for several Reynolds numbers using a grid of 131 × 131. The contour values used here are taken to be the same as those in Lewis (1979), except those on the circular boundary.

Table 1: Flow between rotating circular and fixed square cylinders: Maximum values of the stream function (ψ_{max}) and vorticity (ζ_{max}), and values of the stream function on the circular cylinder (ψ_c) by the present method and FDM.

Re	Method	Grid	ψ_{min}	ψ_{max}	ζ_{max}	ψ_c
1	Present ($\mathbf{u}-p$)	61×61	-1.4203E-4	0.4785	1.0472	0.4785
		81×81	-1.3415E-4	0.4699	1.0233	0.4699
		101×101	-1.3588E-4	0.4712	1.0325	0.4712
		121×121	-1.3523E-4	0.4701	1.0249	0.4701
		131×131	-1.3478E-4	0.4695	1.0216	0.4695
		141×141	-1.3472E-4	0.4691	1.0209	0.4691
	FDM ($\psi-\zeta$) [Lewis (1979)]	161×161	-1.4000E-4	0.4656	1.0186	0.4656
100	Present ($\mathbf{u}-p$)	61×61	-1.2527E-3	0.4808	1.2433	0.4808
		81×81	-1.1994E-3	0.4747	1.2374	0.4747
		101×101	-1.1830E-3	0.4711	1.2265	0.4711
		121×121	-1.1788E-3	0.4679	1.2216	0.4679
		131×131	-1.1760E-3	0.4658	1.2198	0.4658
		141×141	-1.1758E-3	0.4652	1.2193	0.4652
	FDM ($\psi-\zeta$) [Lewis (1979)]	161×161	—	—	—	0.4577
200	Present ($\mathbf{u}-p$)	61×61	-2.0812E-3	0.4777	1.3110	0.4777
		81×81	-1.9988E-3	0.4715	1.3095	0.4715
		101×101	-1.9882E-3	0.4678	1.2992	0.4678
		121×121	-1.9796E-3	0.4652	1.2916	0.4652
		131×131	-1.9721E-3	0.4629	1.2897	0.4629
		141×141	-1.9716E-3	0.4625	1.2893	0.4625
	FDM ($\psi-\zeta$) [Lewis (1979)]	161×161	—	0.4539	1.2559	0.4539
500	Present ($\mathbf{u}-p$)	61×61	-3.0170E-3	0.4738	1.3957	0.4738
		81×81	-2.9114E-3	0.4676	1.4143	0.4676
		101×101	-2.8354E-3	0.4599	1.3732	0.4599
		121×121	-2.7762E-3	0.4526	1.3719	0.4526
		131×131	-2.7298E-3	0.4512	1.3708	0.4512
		141×141	-2.7291E-3	0.4511	1.3702	0.4511
	FDM ($\psi-\zeta$) [Lewis (1979)]	161×161	-2.7100E-3	0.4465	1.3430	0.4465
1000	Present ($\mathbf{u}-p$)	61×61	-3.2525E-3	0.4714	1.4321	0.4714
		81×81	-3.1714E-3	0.4648	1.4899	0.4648
		101×101	-3.1014E-3	0.4502	1.4264	0.4502
		121×121	-3.0326E-3	0.4429	1.3925	0.4429
		131×131	-3.0048E-3	0.4397	1.3767	0.4397
		141×141	-3.0042E-3	0.4394	1.3761	0.4394
	FDM ($\psi-\zeta$) [Lewis (1979)]	161×161	—	—	—	0.4375
1400	Present ($\mathbf{u}-p$)	61×61	-3.2105E-3	0.4707	1.4329	0.4707
		81×81	-3.1543E-3	0.4637	1.5223	0.4637
		101×101	-3.0785E-3	0.4461	1.4279	0.4461
		121×121	-3.0241E-3	0.4379	1.4117	0.4379
		131×131	-2.9953E-3	0.4324	1.4026	0.4324
		141×141	-2.9947E-3	0.4320	1.4024	0.4320
	FDM ($\psi-\zeta$) [Lewis (1979)]	161×161	—	—	—	0.4314

The streamlines of the flow field using a grid of 131×131 is shown in Figure 16, in which the vortices at the corners are well captured and in agreement with the results of Lewis (1979).

4.5 Natural convection in an eccentric annulus between two circular cylinders

The geometry of this problem can be defined through the following parameters: the eccentricity ε, angular position φ, radius of the outer cylinder R_o and radius of the inner cylinder R_i (Figure 17). The inner and outer cylinders are heated $(T_h = 1)$ and cooled $(T_c = 0)$, respectively. Calculation is carried out for $Pr = 0.71$, $R_o/R_i = 2.6$ and $Ra = 10^4$ using a set of uniform grids, namely $\{60\times60, 70\times70, 80\times80, 90\times90, 100\times100\}$ and a set of time steps $\Delta t \in \{0.001, 0.0005, 0.00025, 0.0001\}$. Smaller time steps are used for higher grid densities. A distribution of nodes and the boundary conditions are shown in Figure 17.

For symmetrical flows, where the centres of the inner and outer cylinders lie on the vertical symmetrical axis, several values of eccentricity, namely $\varepsilon \in \{0.25, 0.50, 0.75, 0.95\}$ and angular direction, namely $\varphi \in \{-90^\circ, 90^\circ\}$ are considered. Table 2 compares the maximum value of the stream function (ψ_{max}) between the present scheme, one-dimensional integrated radial basis function (1D-IRBF) scheme [Le-Cao, Mai-Duy, and Tran-Cong (2011)] and differential quadrature method (DQM) [Shu, Yao, Yeo, and Zhu (2002)]. It can be seen that good agreement is achieved. The present solutions are convergent at the grid of 90×90.

For unsymmetrical flows, the stream function at the inner wall (ψ_w) is no longer zero and its value varies with the location of the inner cylinder. Values of the eccentricity and angular direction are taken as $\{0.25, 0.50, 0.75\}$ and $\{-45^\circ, 0^\circ, 45^\circ\}$, respectively. In Table 3, values of ψ_w are presented and agree satisfactorily with those obtained by the 1D-IRBF scheme [Le-Cao, Mai-Duy, and Tran-Cong (2011)], DQM [Shu, Yao, Yeo, and Zhu (2002)] and domain-free discretisation method (DFD) [Shu and Wu (2002)]. It is noted that the present governing equations (1)-(3) are different from those used in Shu, Yao, Yeo, and Zhu (2002) and Shu and Wu (2002) by a factor $\sqrt{PrRa}$. Therefore, to facilitate a comparison, our results in the table, which are computed in the average sense from the values of ψ at the Lagrangian nodes, are multiplied by this factor. The present solutions are convergent at the grid of 90×90.

Figures 18-19 and Figures 20-22 show the isotherms and streamlines of the flow for symmetrical and unsymmetrical flows, respectively, where several combinations of eccentricity and angular direction are considered. Each plot contains 22 contour lines whose levels vary linearly from the minimum to maximum values. All plots look very feasible when compared with those obtained by the 1D-IRBF scheme

[Le-Cao, Mai-Duy, and Tran-Cong (2011)], DQM [Shu, Yao, Yeo, and Zhu (2002)] and (DFD) [Shu and Wu (2002)].

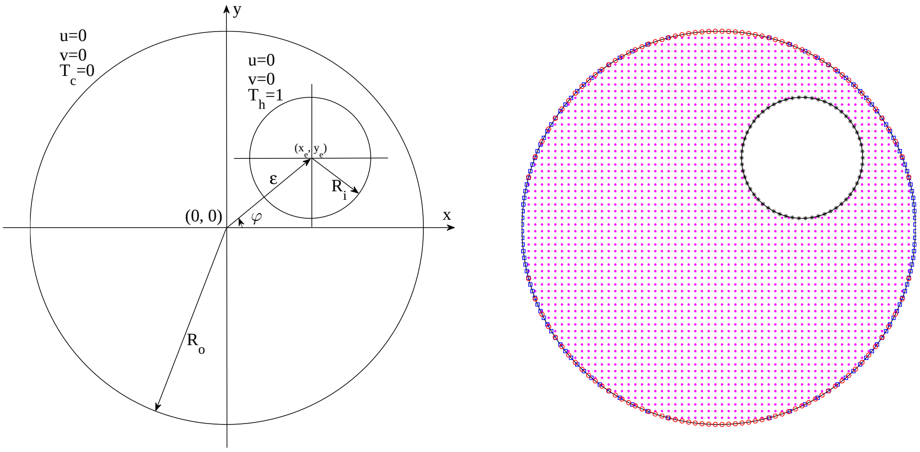

Figure 17: Natural convection in eccentric circular-circular annulus: Geometry and boundary conditions (left) and distribution of nodes (right) (Eulerian nodes inside the annulus and on the outer boundary, Lagrangian nodes on the inner boundary with a grid of 60 × 60).

Table 2: Natural convection in eccentric circular-circular annulus, symmetrical flows: the maximum values of the stream function (ψ_{max}) for two special cases $\varphi \in \{-90^\circ, 90^\circ\}$ by the present and some other numerical schemes.

φ	ε	ψ_{max}						
		DQM[a]	1D-IRBF[b]	DFIB-CIRBF[c]				
				60 × 60	70 × 70	80 × 80	90 × 90	100 × 100
−90°	0.25	15.50	15.71	15.26	15.30	15.35	15.36	15.36
	0.50	18.32	18.50	18.10	18.39	18.44	18.47	18.47
	0.75	20.62	20.72	20.10	20.41	20.47	20.49	20.49
	0.95	22.16	22.19	21.91	22.35	22.44	22.49	22.50
90°	0.25	11.13	11.26	11.07	11.11	11.13	11.14	11.14
	0.50	9.55	9.64	9.51	9.55	9.57	9.58	9.58
	0.75	8.12	8.25	8.17	8.18	8.20	8.21	8.21
	0.95	7.17	7.28	7.21	7.23	7.24	7.24	7.24

[a] Shu, Yao, Yeo, and Zhu (2002)
[b] Le-Cao, Mai-Duy, and Tran-Cong (2011)
[c] Present

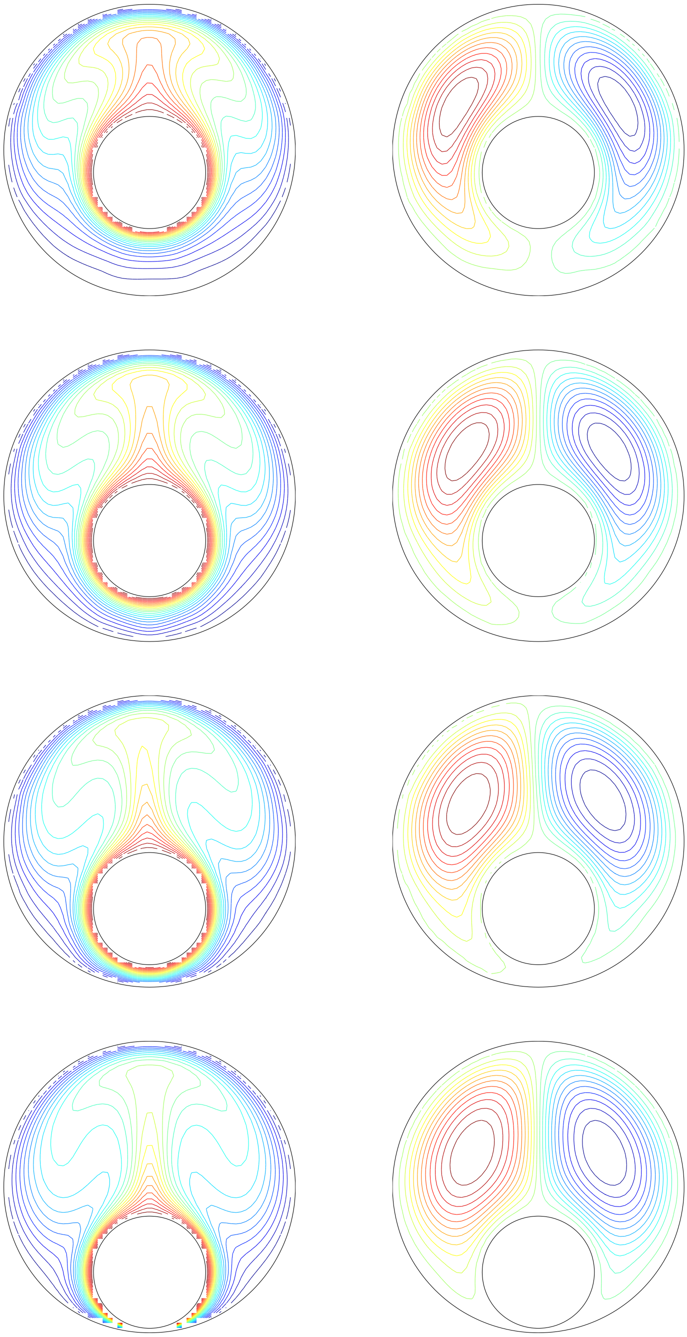

Figure 18: Natural convection in an eccentric circular-circular annulus, symmetrical flows: Contour plots for the temperature (left) and stream function (right) fields for $\varepsilon \in \{0.25, 0.50, 0.75, 0.95\}$ (from top to bottom) and $\varphi = -90^\circ$. Each plot contains 22 contour lines whose levels vary linearly from the minimum to maximum values.

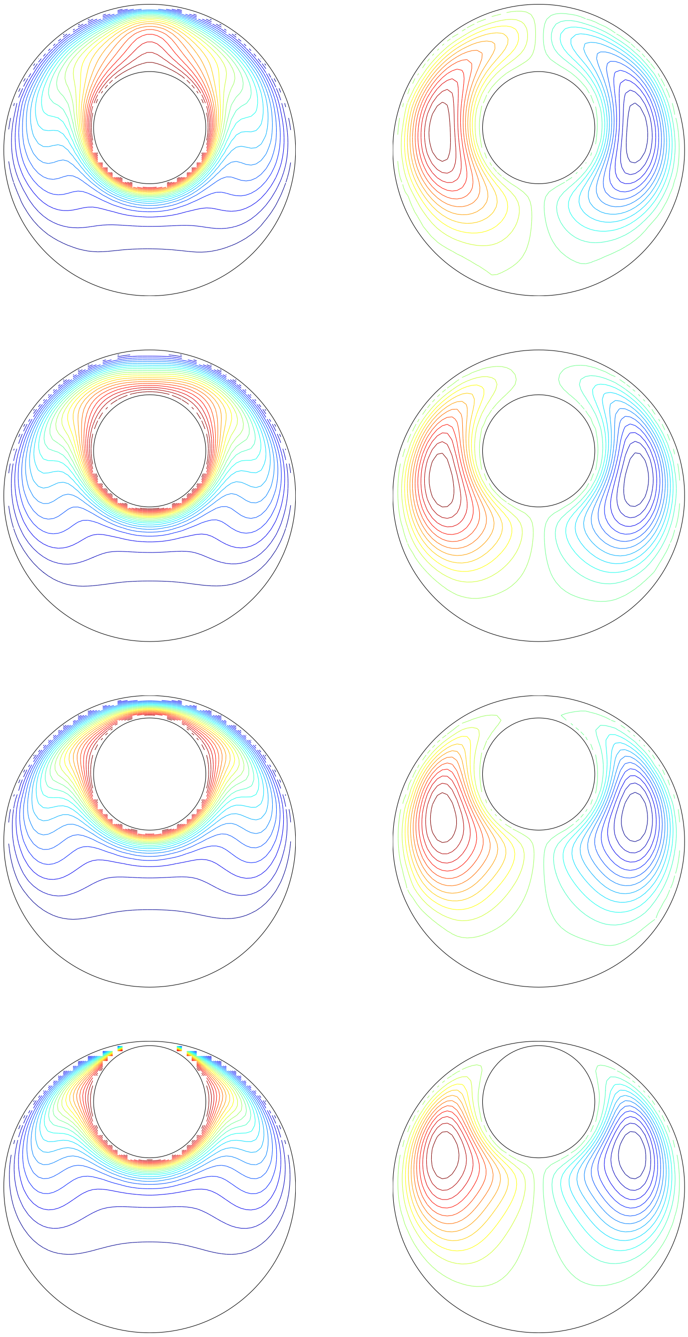

Figure 19: Natural convection in an eccentric circular-circular annulus, symmetrical flows: Contour plots for the temperature (left) and stream function (right) fields for $\varepsilon \in \{0.25, 0.50, 0.75, 0.95\}$ (from top to bottom) and $\varphi = 90^\circ$. Each plot contains 22 contour lines whose levels vary linearly from the minimum to maximum values.

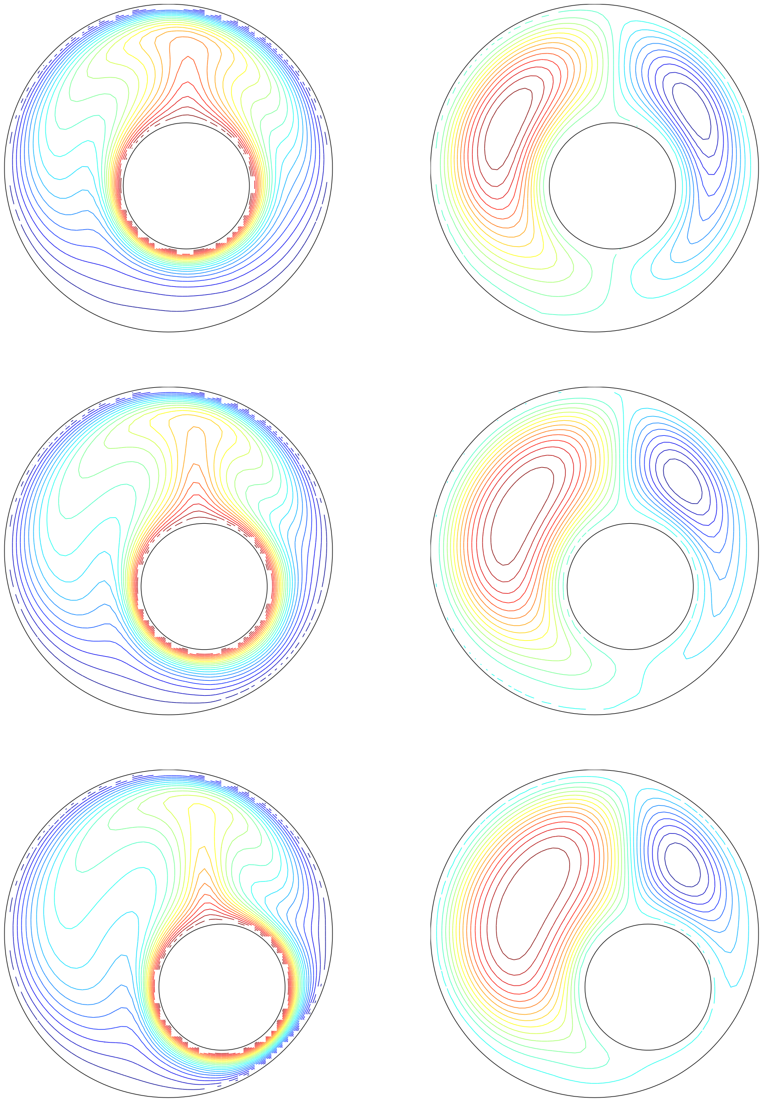

Figure 20: Natural convection in an eccentric circular-circular annulus, unsymmetrical flows: Contour plots for the temperature (left) and stream function (right) fields for $\varepsilon \in \{0.25, 0.50, 0.75\}$ (from top to bottom) and $\varphi = -45^\circ$. Each plot contains 22 contour lines whose levels vary linearly from the minimum to maximum values.

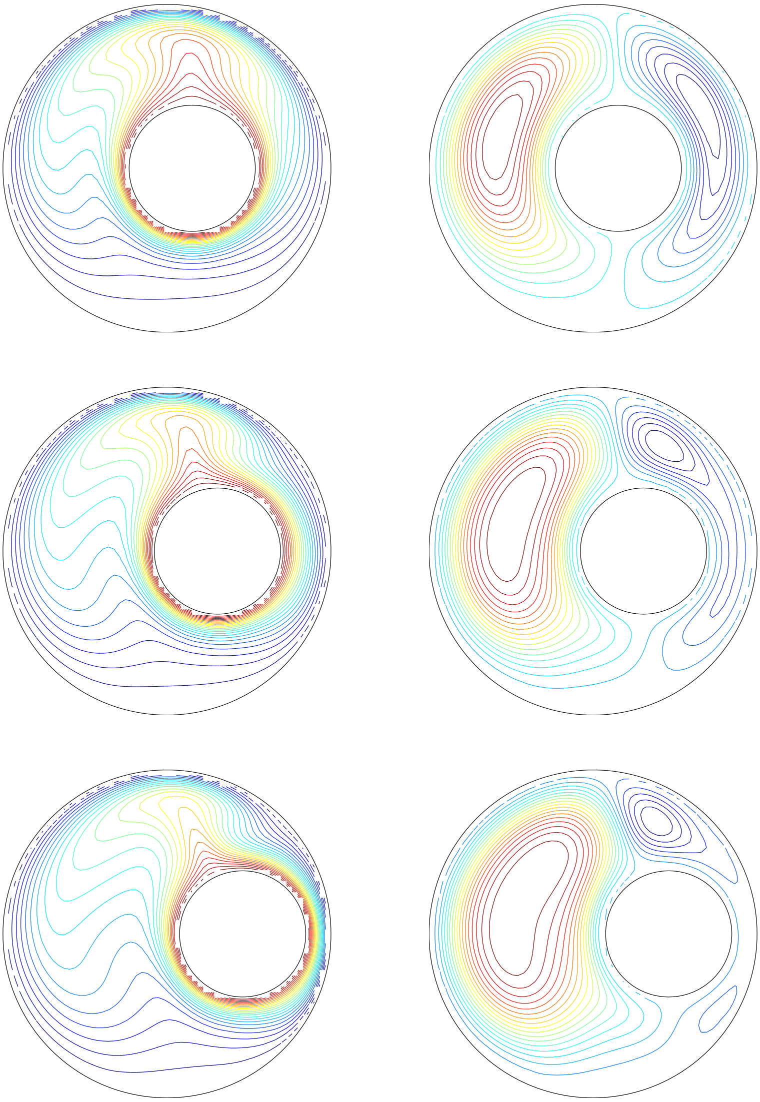

Figure 21: Natural convection in an eccentric circular-circular annulus, unsymmetrical flows: Contour plots for the temperature (left) and stream function (right) fields for $\varepsilon \in \{0.25, 0.50, 0.75\}$ (from top to bottom) and $\varphi = 0^\circ$. Each plot contains 22 contour lines whose levels vary linearly from the minimum to maximum values.

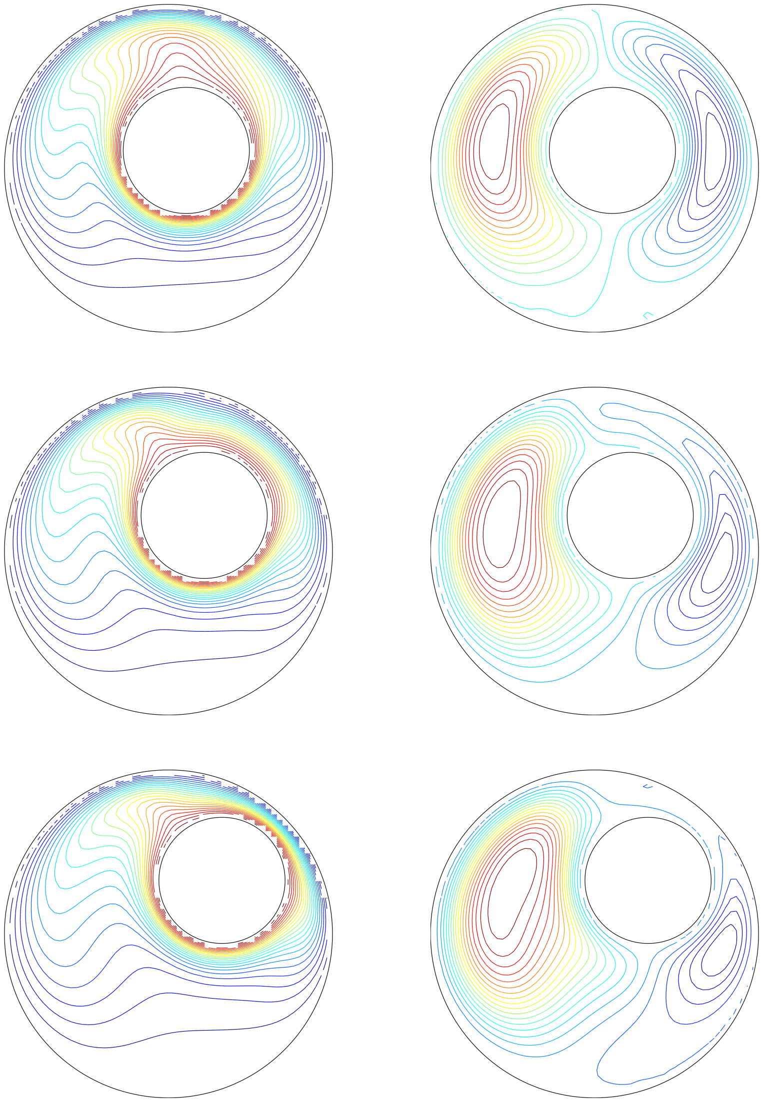

Figure 22: Natural convection in an eccentric circular-circular annulus, unsymmetrical flows: Contour plots for the temperature (left) and stream function (right) fields for $\varepsilon \in \{0.25, 0.50, 0.75\}$ (from top to bottom) and $\varphi = 45^\circ$. Each plot contains 22 contour lines whose levels vary linearly from the minimum to maximum values.

Table 3: Natural convection in eccentric circular-circular annulus, unsymmetrical flows: the stream function values at the inner cylinders (ψ_w) for $\varepsilon \in \{0.25, 0.50, 0.75\}$ and $\varphi \in \{-45°, 0°, 45°\}$ by the present and some other numerical schemes.

		ψ_w							
φ	ε	DFD[a]	DQM[b]	1D-IRBF[c]	DFIB-CIRBF[d]				
					60×60	70×70	80×80	90×90	100×100
−45°	0.25	0.51	0.51	0.48	0.46	0.48	0.49	0.50	0.50
	0.50	0.77	0.92	0.80	0.80	0.81	0.82	0.82	0.82
	0.75	0.77	0.99	1.05	1.10	1.13	1.14	1.15	1.15
0°	0.25	0.72	0.72	0.60	0.67	0.68	0.68	0.68	0.68
	0.50	1.10	1.15	1.28	1.07	1.07	1.07	1.07	1.07
	0.75	1.26	1.30	1.18	1.25	1.29	1.31	1.32	1.32
45°	0.25	0.54	0.52	0.52	0.56	0.57	0.57	0.57	0.57
	0.50	1.29	1.31	1.25	1.23	1.23	1.23	1.23	1.23
	0.75	1.09	1.07	1.01	0.98	1.01	1.02	1.03	1.03

[a] Shu and Wu (2002)

[b] Shu, Yao, Yeo, and Zhu (2002)

[c] Le-Cao, Mai-Duy, and Tran-Cong (2011)

[d] Present

5 Concluding remarks

In this paper, we introduce compact integrated RBF approximations into the immersed boundary and point-collocation framework to simulate viscous flows in two dimensions. The direct forcing immersed boundary method is utilised for the handling of inner boundaries, while high-order approximation schemes (Adams-Bashforth/Crank-Nicolson and compact 3-point IRBFs) are employed to represent temporal and spatial derivatives. The proposed method is verified successfully in a series of fluid flow problems in multiply-connected domains. Very good results are obtained using relatively coarse Cartesian grids.

Acknowledgement: Thai-Quang would like to thank USQ, FoES and CESRC for a postgraduate research scholarship. This work was supported by the Australian Research Council.

References

Botella, O.; Peyret, R. (1998): Benchmark spectral results on the lid-driven cavity flow. *Computers & Fluids*, vol. 27, no. 4, pp. 421–433.

Butcher, J. C. (2003): *Numerical Methods for Ordinary Differential Equations*. John Wiley.

Crank, J.; Nicolson, P. (1996): A practical method for numerical evaluation of solutions of partial differential equations of the heat-conduction type. *Advances in Computational Mathematics*, vol. 6, no. 1, pp. 207–226.

Ding, H.; Shu, C.; Yeo, K.; Xu, D. (2006): Numerical computation of three-dimensional incompressible viscous flows in the primitive variable form by local multiquadric differential quadrature method. *Computer Methods in Applied Mechanics and Engineering*, vol. 195, no. 7-8, pp. 516–533.

Fadel, H.; Agouzoul, M. (2011): High-order finite difference schemes for incompressible flows. *International Journal for Numerical Methods in Fluids*, vol. 65, no. 9, pp. 1050–1070.

Fadlun, E. A.; Verzicco, R.; Orlandi, P.; Mohd-Yusof, J. (2000): Combined immersed-boundary finite-difference methods for three-dimensional complex flow simulations. *Journal of Computational Physics*, vol. 161, no. 1, pp. 35–60.

Franke, R. (1982): Scattered data interpolation: Tests of some method. *Mathematics of Computation*, vol. 38, pp. 181–200.

Goldstein, D.; Handler, R.; Sirovich, L. (1993): Modeling a no-slip flow boundary with an external force field. *Journal of Computational Physics*, vol. 105, no. 2, pp. 354–366.

Ji, C.; Munjiza, A.; Williams, J. (2012): A novel iterative direct-forcing immersed boundary method and its finite volume applications. *Journal of Computational Physics*, vol. 231, no. 4, pp. 1797–1821.

Kansa, E. J. (1990): Multiquadrics- A scattered data approximation scheme with applications to computational fluid-dynamics-I. surface approximations and partial derivative estimates. *Computers and Mathematics with Applications*, vol. 19, no. 8/9, pp. 127–145.

Kim, J.; Kim, D.; Choi, H. (2001): An immersed-boundary finite-volume method for simulations of flow in complex geometries. *Journal of Computational Physics*, vol. 171, no. 1, pp. 132–150.

Kim, J.; Moin, P. (1985): Application of a fractional-step method to incompressible navier-stokes equations. *Journal of Computational Physics*, vol. 59, no. 2, pp. 308–323.

Le, D. V.; Khoo, B. C.; Peraire, J. (2006): An immersed interface method for viscous incompressible flows involving rigid and flexible boundaries. *Journal of Computational Physics*, vol. 220, no. 1, pp. 109–138.

Le-Cao, K.; Mai-Duy, N.; Tran-Cong, T. (2009): An effective integrated-RBFN Cartesian-grid discretization for the stream function-vorticity-temperature formulation in nonrectangular domains. *Numerical Heat Transfer, Part B: Fundamentals*, vol. 55, no. 6, pp. 480–502.

Le-Cao, K.; Mai-Duy, N.; Tran-Cong, T. (2011): Numerical study of stream-function formulation governing flows in multiply-connected domains by integrated rbfs and cartesian grids. *Computers & Fluids*, vol. 44, no. 1, pp. 32–42.

Leveque, R. J.; Li, Z. (1994): The immersed interface method for elliptic equations with discontinuous coefficients and singular sources. *SIAM Journal on Numerical Analysis*, vol. 31, no. 4, pp. 1019–1044.

Lewis, E. (1979): Steady flow between a rotating circular cylinder and fixed square cylinder. *Journal of Fluid Mechanics*, vol. 95, pp. 497–513.

Mai-Duy, N.; Le-Cao, K.; Tran-Cong, T. (2008): A Cartesian grid technique based on one-dimensional integrated radial basis function networks for natural convection in conccentric annuli. *International Journal for Numerical Methods in fluids*, vol. 57, pp. 1709–1730.

Mai-Duy, N.; Tanner, R. I. (2007): A collocation method based on one-dimensional rbf interpolation scheme for solving pdes. *International Journal of Numerical Methods for Heat & Fluid Flow*, vol. 17, no. 2, pp. 165–186.

Mai-Duy, N.; Tran-Cong, T. (2001): Numerical solution of differential equations using multiquadric radial basic function networks. *Neural Networks*, vol. 14, pp. 185–199.

Mai-Duy, N.; Tran-Cong, T. (2001): Numerical solution of Navier-Stokes equations using multiquadric radial basis function networks. *International Journal for Numerical Methods in Fluids*, vol. 37, no. 1, pp. 65–86.

Mai-Duy, N.; Tran-Cong, T. (2008): Integrated radial-basis-function networks for computing newtonian and non-newtonian fluid flows. *Computers & Structures*, vol. 87, no. 11-12, pp. 642–650.

Mai-Duy, N.; Tran-Cong, T. (2011): Compact local integrated-rbf approximations for second-order elliptic differential problems. *Journal of Computational Physics*, vol. 230, no. 12, pp. 4772–4794.

Mai-Duy, N.; Tran-Cong, T. (2013): A compact five-point stencil based on integrated rbfs for 2d second-order differential problems. *Journal of Computational Physics*, vol. 235, pp. 302–321.

Mittal, R.; Iaccarino, G. (2005): Immersed boundary methods. *Annual Review of Fluid Mechanics*, vol. 37, no. 1, pp. 239–261.

Peskin, C. S. (1977): Numerical analysis of blood flow in the heart. *Journal of Computational Physis*, vol. 25, pp. 220–252.

Peskin, C. S. (2002): The immersed boundary method. *Acta Numerica*, vol. 11, pp. 479–517.

Roma, A. M.; Peskin, C. S.; Berger, M. J. (1999): An adaptive version of the immersed boundary method. *Journal of Computational Physics*, vol. 153, no. 2, pp. 509–534.

Saiki, E. M.; Biringen, S. (1996): Numerical simulation of a cylinder in uniform flow: Application of a virtual boundary method. *Journal of Computational Physics*, vol. 123, no. 2, pp. 450–465.

Sanmiguel-Rojas, E.; Ortega-Casanova, J.; del Pino, C.; Fernandez-Feria, R. (2005): A cartesian grid finite-difference method for 2d incompressible viscous flows in irregular geometries. *Journal of Computational Physics*, vol. 204, no. 1, pp. 302–318.

Shu, C.; Wu, Y. L. (2002): Domain-free discretization method for doubly connected domain and its application to simulate natural convection in eccentric annuli. *Computer Methods in Applied Mechanics and Engineering*, vol. 191, no. 17-18, pp. 1827–1841.

Shu, C.; Yao, Q.; Yeo, K. S.; Zhu, Y. D. (2002): Numerical analysis of flow and thermal fields in arbitrary eccentric annulus by differential quadrature method. *Journal of Heat and Mass Transfer*, vol. 38, pp. 597–608.

Su, S.-W.; Lai, M.-C. (2007): An immersed boundary technique for simulating complex flows with rigid boundary. *Computers & Fluids*, vol. 36, no. 2, pp. 313–324.

Thai-Quang, N.; Le-Cao, K.; Mai-Duy, N.; Tran-Cong, T. (2012): A high-order compact local integrated-rbf scheme for steady-state incompressible viscous flows in the primitive variables. *CMES: Computer Modeling in Engineering & Sciences*, vol. 84, no. 6, pp. 528–558.

Thai-Quang, N.; Mai-Duy, N.; Tran, C.-D.; Tran-Cong, T. (2012): High-order alternating direction implicit method based on compact integrated-rbf approximations for unsteady/steady convection-diffusion equations. *CMES: Computer Modeling in Engineering & Sciences*, vol. 89, no. 3, pp. 189–220.

Tian, Z.; Liang, X.; Yu, P. (2011): A higher order compact finite difference algorithm for solving the incompressible navier-stokes equations. *International Journal for Numerical Methods in Fluids*, vol. 88, pp. 511–532.

Uhlmann, M. (2005): An immersed boundary method with direct forcing for the simulation of particulate flows. *Journal of Computational Physics*, vol. 209, no. 2, pp. 448 – 476.

Wang, Z.; Fan, J.; Luo, K. (2008): Combined multi-direct forcing and immersed boundary method for simulating flows with moving particles. *International Journal of Multiphase Flow*, vol. 34, no. 3, pp. 283–302.